

A11104 608795

NIST
PUBLICATIONS

NISTIR 5645

Evaluation of Thermal Wave Imaging for Detection of Machining Damage in Ceramics

**L. Wei
H.H.K. Xu
S. Jahanmir**

U.S. DEPARTMENT OF COMMERCE
Technology Administration
National Institute of Standards
and Technology
Gaithersburg, MD 20899

QC
100
.U56
NO.5645
1995

NIST

Evaluation of Thermal Wave Imaging for Detection of Machining Damage in Ceramics

**L. Wei
H.H.K. Xu
S. Jahanmir**

U.S. DEPARTMENT OF COMMERCE
Technology Administration
National Institute of Standards
and Technology
Gaithersburg, MD 20899

March 1995



U.S. DEPARTMENT OF COMMERCE
Ronald H. Brown, Secretary

TECHNOLOGY ADMINISTRATION
Mary L. Good, Under Secretary for Technology

NATIONAL INSTITUTE OF STANDARDS
AND TECHNOLOGY
Arati Prabhakar, Director

1. Introduction

2. Methodology

3. Results

4. Conclusion

SUMMARY

The feasibility of a thermal wave imaging technique is evaluated for the detection and characterization of machining damage in ceramics. First, a well-defined crack system produced by Vickers indentation is used to examine the characteristic response of thermal wave signals to different forms of cracks (i.e., median/radial and lateral). The results clearly indicate that thermal wave imaging can be used for the detection of surface and subsurface cracks in ceramics. Thermal wave imaging is then conducted on the surfaces of ground alumina and the cross-section of scratched silicon nitride. Careful examinations of the thermal wave images confirm that this technique can be used to detect the grinding-induced subsurface microcracks. The thermal wave measurement results also lead to a quantitative estimation of the density of grinding-induced microcracks. This study demonstrates that the thermal wave technique is a feasible non-destructive evaluation method for the detection of machining damage in ceramics. The principle of operation and the experimental procedures of the thermal wave imaging technique are described in the report. The limitations of the thermal wave imaging technique in the detection of small cracks and precautions regarding choosing appropriate sets of imaging parameters are pointed out.

ACKNOWLEDGEMENT

This project was conducted under the auspices of the Ceramic Machining Consortium, which is a joint research program between NIST, industry, universities, and government agencies. The financial support received from the Ceramic Technology Project (DOE office of Transportation Technologies) under contract DE-ACO5-84OR21400 with Martin Marietta Energy Systems, Inc., and Office of Intelligent Processing of Materials (NIST Materials Science and Engineering Laboratory) are gratefully acknowledged. The authors are grateful to Dr. G. White and Dr. B. Lawn for fruitful discussions.

TABLE OF CONTENTS

	Page
SUMMARY	1
ACKNOWLEDGEMENTS	2
INTRODUCTION	5
MEASUREMENT PRINCIPLE AND SYSTEM	5
EXPERIMENTAL RESULTS	7
DISCUSSION AND CONCLUSIONS	12
REFERENCES	16
Appendix 1	
“Non-Destructive Detection of Damage Produced by a Sharp Indenter in Ceramics”	18
Appendix 2	
“Effect of Grain Size on Grinding Damage in Alumina”	49
Appendix 3	
“Grinding Force and Microcrack Density in Abrasive Machining of Silicon Nitride”	83

I. INTRODUCTION

Machining-induced damage is often a limiting factor in determining the strength and reliability of ceramic materials in engineering applications [1]. A particular type of machining damage that is detrimental to the performance of ceramic components consists of microcracks at and below the machined surfaces [2-6]. Evaluation of this damage, preferably in a non-destructive manner, is therefore important for both manufacturing quality control and as a fundamental study of material removal mechanisms.

There has been a substantial effort devoted to the development of non-destructive evaluation techniques, such as thermal wave imaging [7,8], ultrasonic detection [9,10], and micro-radiography [11]. The characteristic features (i.e., size and location) of machining-induced microcracks, however, make the application of these techniques to machining difficult. These microcracks usually extend only to a few tens of micrometers below the machined surfaces. Therefore, detection of such damage requires an evaluation technique that has a high sensitivity to small subsurface microcracks, with a low sensitivity to the roughness of the machined surfaces. It is in this context that thermal wave imaging may be beneficial for the characterization of machining damage in ceramics.

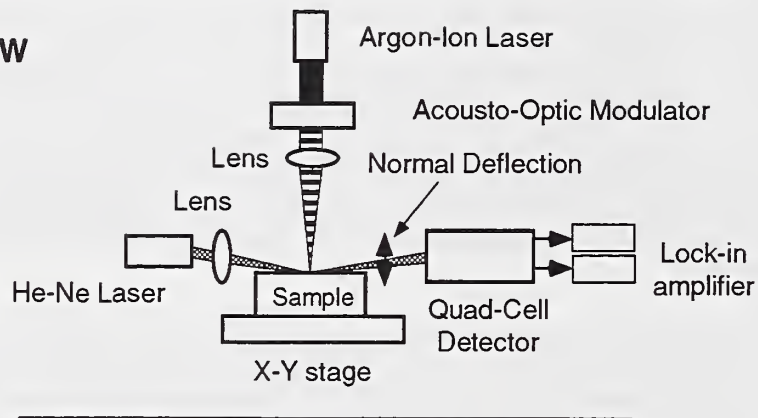
The goal of this project was to evaluate the feasibility of a thermal wave technique (i.e., the photothermal deflection method), for the detection and characterization of machining damage in ceramics. To accomplish this goal, we first applied the thermal wave technique to well-defined surface and subsurface cracks produced by indentation. After establishing the detectability of cracks with known forms [12], we applied the thermal wave technique to ground ceramic surfaces for the detection and quantification of machining-induced microcracks [13,14]. This report summarizes the research results obtained during the past two years in establishing the feasibility of the thermal wave technique for the evaluation of machining damage in ceramics. A more detailed description of the test procedures and the results is included in the appendices.

II. MEASUREMENT PRINCIPLE AND SYSTEM

In general, thermal wave techniques are based on the measurement of the temperature distribution (both in time and in space) generated by heating the material under evaluation. The thermal wave technique used in this research is the optical beam deflection method (also called the "mirage effect method") [15]. In this technique, the specimen is locally heated by a modulated laser beam, which generates a changing temperature distribution (i.e., thermal waves) in the specimen and in the air above the specimen. The thermal waves in the air cause a modulated change in the index of refraction. The temperature distribution in the solid is then detected by measuring the deflection of a laser probe beam passing through the air in close proximity to the sample surface. This method is sufficiently sensitive for the detection of microcracks because of the changes in the local heat flux due to the interruption of phonon propagation by microcracks. Since the thermal wave penetration depth depends on the thermal diffusivity of the material and the modulation frequency of the periodic heat source, the detection depth for a given material can be controlled by adjusting the modulation frequency. Generally speaking, the lower the modulation frequency or the higher the diffusivity, the larger is the penetration depth.

A schematic diagram of the experimental setup is shown in Fig.1. An argon-ion laser beam is chopped by an acousto-optic modulator and is focused on the sample surface to provide a periodic localized heat source. The He-Ne laser probe beam bounces at a near grazing angle from the surface of the heating area; and it is refracted by the time varying gradient in the index of refraction

SIDE VIEW



TOP VIEW

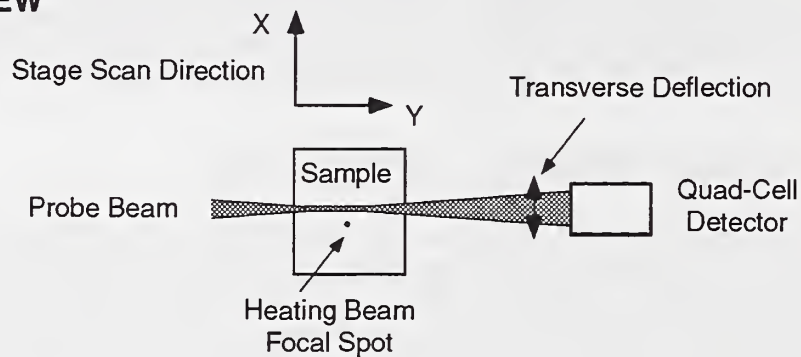


Figure 1. Schematic diagram of the thermal wave measurement system with the optical beam deflection technique [16].

of the air caused by the temperature gradient. The vector deflection of the probe beam is measured by a position-sensitive, quad-cell detector, the output voltages of which are amplified and fed into two separate vector lock-in amplifiers: one to monitor the component normal to the surface (i.e., the normal deflection), and the other to monitor the deflection parallel to the surface (i.e., the transverse deflection).

In the thermal wave measurements presented in this report, the radius of the heating beam was 10 μm and that of the probe beam was 15 μm . An x-y stage, controlled by a personal computer, was used to move the sample relative to the Argon-ion laser beam in order to obtain a thermal wave image of a region under investigation. The voltage signals obtained from the lock-in amplifiers were converted to digital data and were plotted using a commercial graphics software.

III. EXPERIMENTAL RESULTS

The thermal wave imaging technique was first applied to a well-defined crack system to establish the detection capability of this technique [12]. Once it was determined that both surface and subsurface cracks could be detected, ground surfaces of alumina and scratched cross-sections of silicon nitride were examined by thermal wave imaging to analyze for microcracks generated by grinding and by scratching.

1. Detection of Indentation Damage

The cracks generated by Vickers indentation were chosen for this study because similar cracks may form by grinding of brittle ceramics [3]. In addition, the two cracks (i.e., median/radial and lateral cracks) are well-defined [17]. Although the indentation cracks may be larger than most microcracks formed by grinding, this crack system serves as a baseline for the evaluation of the thermal wave technique.

Two types of materials were selected for this study: a hot-isostatically pressed silicon nitride (NBD200, Norton Company, Northboro, MA)* and a soda-lime glass. The thermal conductivity of these two materials differ by two orders of magnitude, with the former having the larger value. Both materials were polished for the study of indentation cracks to reduce the influence of surface roughness on the measurements.

Figure 2a shows the impression made on the glass specimen under an indentation load of 9.8 N. The median/radial cracks emanating from the corners of the indent are also shown. The thermal wave image using the transverse deflection component is shown in Fig. 2b. The transverse deflection component of the probe beam was used for the detection of the median/radial cracks because the transverse deflection component is more sensitive to the thermal waves with preferential propagation along the surface and perpendicular to the vertical crack plane [7]. In the image shown in Fig. 2b, the median/radial cracks appear darker than the background because of local temperature rise due to the reflection of thermal waves from the cracks. The Y-shape of the median/radial cracks can be clearly seen, while the lateral cracks and the depression of the indent are only vaguely seen in the background. It is important to note that the cracks along the x-direction are located in a plane parallel to the heat propagation direction and do not disturb the heat flow; therefore, these cracks are not detected in the thermal wave image of Fig. 2b.

* Information on product names, manufacturers and suppliers is included in this report for clarity. This does not imply endorsement by the National Institute of Standards and Technology.

Figure 3a is a schematic drawing of the indentation mark made at a load of 98 N in the silicon nitride specimen. Both the impression and the well-developed median/radial cracks are shown. Figure 3b and 3c are the corresponding thermal wave images using the transverse and the normal components of the deflected probe beam, respectively. Similar to the results obtained for the glass specimen, the thermal wave image in Fig. 3b shows only the median/radial cracks located in the y-direction. Figure 3c, on the other hand, shows the lateral cracks only, because the normal deflection component is more sensitive to the cracks that are parallel to the surface.

These results clearly show that thermal wave imaging can be used for the detection of surface and subsurface cracks in ceramics. An important feature of this technique is the fact that the different deflection components of the probe beam can be used for the detection of cracks that may be either vertical or parallel to the surface. The transverse deflection component can be used for the detection of median/radial cracks, whereas the normal deflection component can be used for the detection of lateral cracks.

2. Detection and Quantification of Grinding-Induced Damage

Five polycrystalline alumina specimens with average grain sizes of 3, 9, 15, 21 and 35 μm were used for this part of study [13]. Grinding was performed with a 320 grit diamond wheel using a wheel surface speed of 37 $\text{m}\cdot\text{s}^{-1}$, a table speed of 0.12 $\text{m}\cdot\text{s}^{-1}$, and a depth of cut of 40 $\mu\text{m}/\text{pass}$.

Figure 4 shows a series of thermal wave images taken on the ground surfaces of the alumina samples using the normal component of the deflected beam. These images were prepared with the same contrast to allow a comparison between the signals obtained from all the samples. The thermal wave images in Fig. 4 show darker spots corresponding to signals of larger amplitude generated as a result of localized high-temperature regions. The following examinations were conducted to confirm that the dark spots (or the high-temperature regions) in the thermal wave images correspond to subsurface grinding-induced damage [13]:

- (1) Polished samples were examined as reference. During polishing a sufficient thickness of material was removed to ensure that the samples were free of machining damage. The results of thermal wave analysis showed a uniform temperature field, eliminating the possibility that the high-temperature regions in Fig. 4 were associated with microstructural features.
- (2) SEM micrographs and thermal wave images taken from the same areas on the ground surfaces were compared. There was no correlation between the high-temperature regions in the thermal wave images and the grain pullout pits observed in the SEM micrographs, indicating that the high-temperature regions in the thermal wave images were not generated by surface related features such as pits.
- (3) Different modulation frequencies were used to vary the penetration depth of the thermal waves. The thermal wave images in Figs. 5a and 5b were obtained at two different frequencies of 50 kHz and 500 Hz. The two thermal wave images correspond to penetration depths of $\approx 10\ \mu\text{m}$ and $\approx 100\ \mu\text{m}$, respectively from the same area on the ground surface of the alumina with an average grain size of 35 μm . Only a few high-temperature regions are observed in the thermal wave image which corresponds to a penetration depth of $\approx 10\ \mu\text{m}$ (Fig. 5a). In contrast with this observation, several dark spots are seen in Fig. 5b obtained from a penetration depth of $\approx 100\ \mu\text{m}$. The comparison between the two images implies that the high-temperature regions in Fig. 5b are associated with subsurface damage

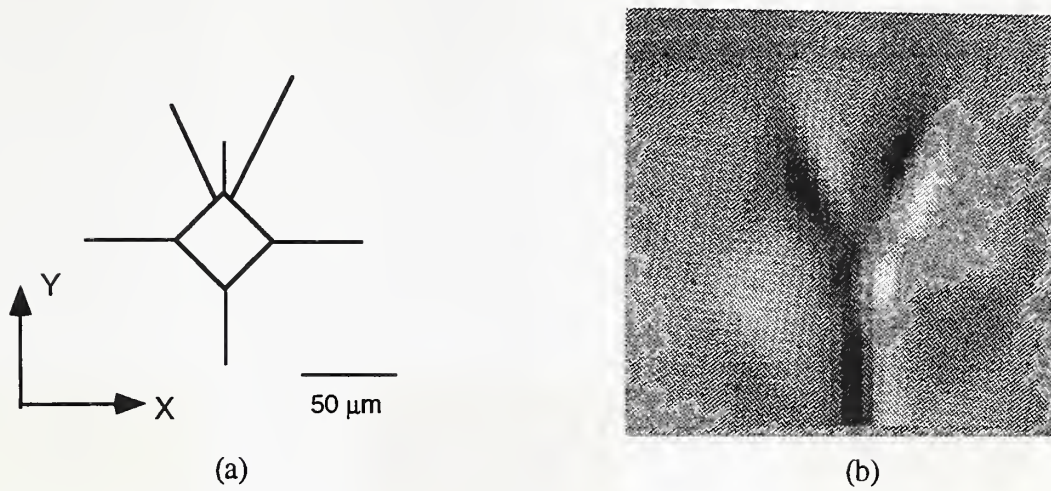


Figure 2. (a) Schematic drawing of the indentation mark on soda-lime glass, and (b) thermal wave image of the indentation mark using the transverse deflection component of the probe beam. (The scan area is $200\text{ }\mu\text{m} \times 200\text{ }\mu\text{m}$ with a step size of $5\text{ }\mu\text{m}$ in both x and y directions).

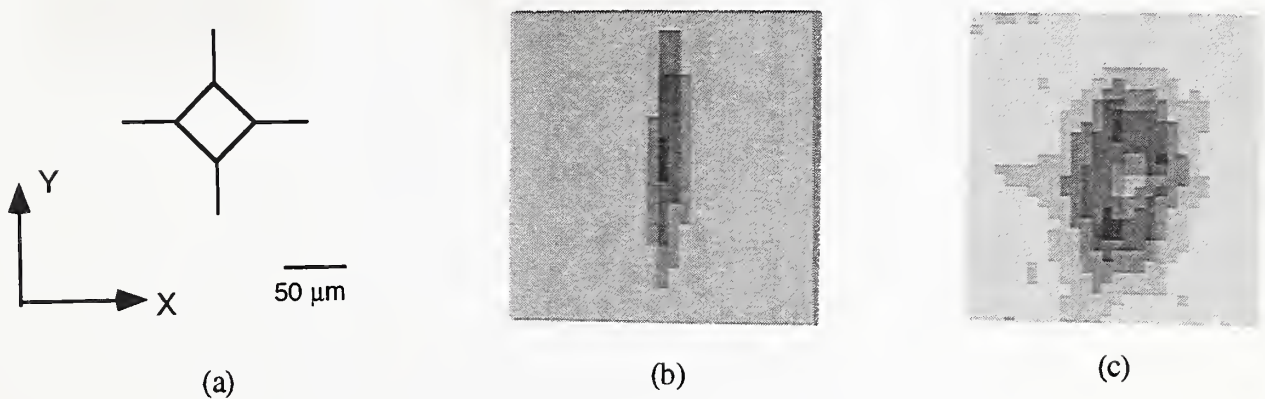
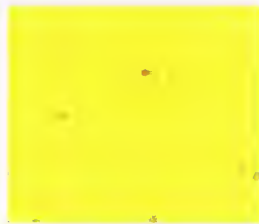
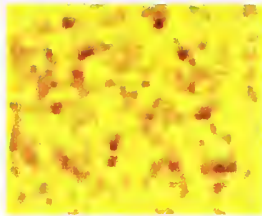


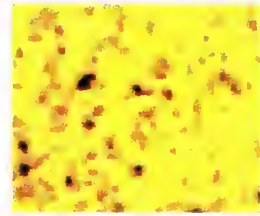
Figure 3. (a) Schematic drawing of the indentation mark on silicon nitride, (b) thermal wave image of the indentation mark using the transverse deflection component of the probe beam, and (c) thermal wave image of the same area using the normal deflection component. (The scan area for both images in (b) and (c) is $300\text{ }\mu\text{m} \times 300\text{ }\mu\text{m}$ with a step size of $10\text{ }\mu\text{m}$ in both x and y directions).



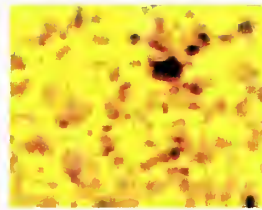
a



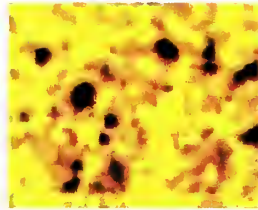
b



c

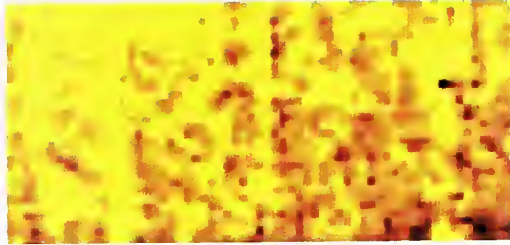


d

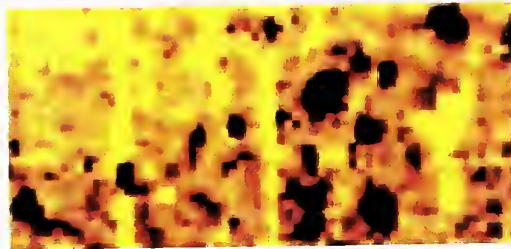


e

Figure 4. Thermal wave images of ground alumina specimens with grain sizes (a) 3, (b) 9, (c) 15, (d) 21, and (e) 35 μm , using the normal component of the deflected probe beam. The scan area of each image is 450 μm x 380 μm .



(a)



(b)

Figure 5. Thermal wave images of the ground surface of alumina with an average grain size of 35 μm examined at a modulation frequency of (a) 50 kHz and (b) 500 Hz using the normal component of the deflected probe beam. The scan area of each image is 500 μm x 250 μm .

located at a depth between 10 and 100 μm .

These results support the conclusion that the dark spots shown in the thermal wave images are associated with grinding-induced subsurface microcracks. Note that the thermal wave images were obtained from the normal component of the deflected probe beam, hence the results are not very sensitive to cracks that are exactly perpendicular to the surface. Therefore, the high-temperature regions observed in the thermal wave images in Figs. 4 and 5 correspond to those subsurface microcracks that are not perpendicular to the ground surface.

Measurement of the area fraction of the dark spots in the thermal wave images can be used to estimate the density of grinding-induced subsurface microcracks. This is accomplished by first estimating the total area of the dark spots in a thermal wave image having a signal amplitude larger than a chosen threshold and dividing this value by the total area of the thermal wave image. The result of this calculation is plotted in Fig. 6, which indicates that the density of subsurface microcracks is related to the inverse square root of the grain size. This functional relationship agrees with the prediction of a microcracking model [18].

3. Quantification of Scratching-Induced Microcrack Density

The thermal wave imaging technique also can be used, together with the bonded-interface sectioning technique [6], to investigate the fundamental process of material removal in machining [14]. Two forms of silicon nitride were selected for this study, namely, a “fine-grain” silicon nitride, with an average grain diameter of 0.5 μm and length of 2 μm , and a “coarse-grain” silicon nitride, with an average grain diameter of 2 μm and length of 8 μm . The polished surfaces of two specimens of each material were bonded together and the top surfaces were ground and polished. Scratches were made normal to the bonded interface on the polished surfaces with a conical diamond indenter under a constant load of 60 N. After scratching, the two specimens were separated and subsurface damage was examined using optical microscopy.

The subsurface damage generated by scratching are observed in the optical micrographs of the sections in Figs. 7a and 7b. Figures 7c and 7d show the thermal wave images of the sections using the normal deflection component of the probe beam, while Figs. 7e and 7f are the thermal wave images using the transverse component. Note the correspondence between these thermal wave images and the optical micrographs. The median cracks (designated by “m”) are more clear in Figs. 7e and 7f than in Figs. 7b and 7c because the transverse deflection component is more sensitive to vertical cracks. On the other hand, Figs. 7c and 7d show strong signals from the damage zone. We have shown in a previous publication that the damage zone associated with scratching contains numerous intergranular microcracks with different orientations [14]. Therefore, the thermal wave images obtained from the normal deflection component reflects the integrated effect of the microcracks distributed within the damage zone.

IV. DISCUSSION AND CONCLUSIONS

The thermal wave imaging technique evaluated in this investigation can be used for the non-destructive detection of grinding-induced microcracks and for quantification of the density of microcracks. However, some limitations of the thermal wave imaging system in crack detection should be recognized. First, the thermal wave measurement technique may not be effective in detecting tightly closed cracks since the heat flow is not greatly disturbed by such cracks. The second issue is related to the orientation of the crack plane with respect to the heat propagation direction. The thermal wave images obtained from the normal component of the deflected probe

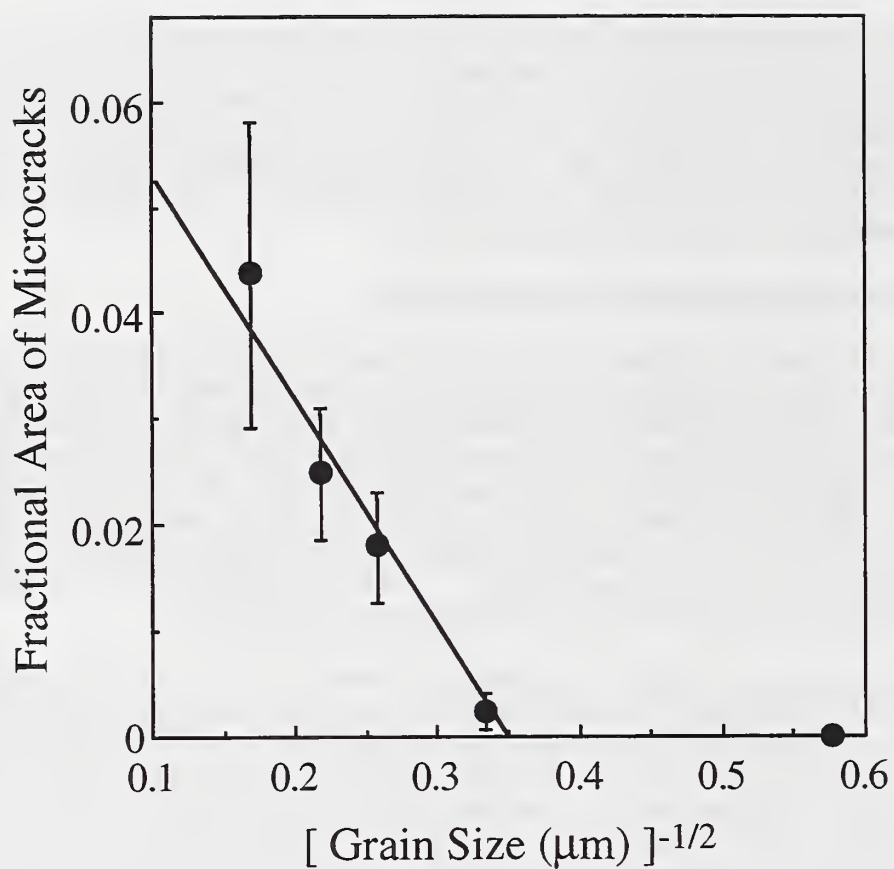
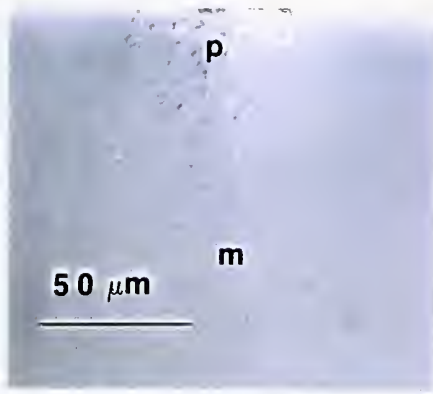
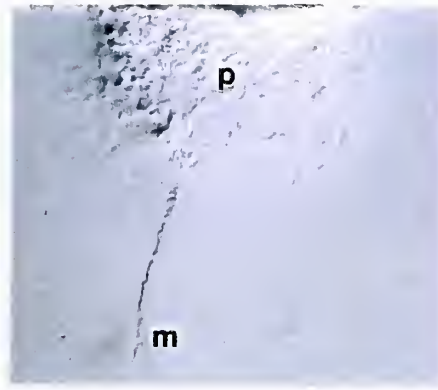


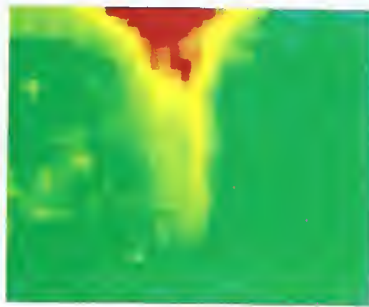
Figure 6. Fractional area of subsurface microcracks (or microcrack density) in ground alumina, measured by thermal wave imaging, plotted versus the inverse square root of the grain size. Each data point is the average of four measurements and the error bars are the standard deviation of the measurements.



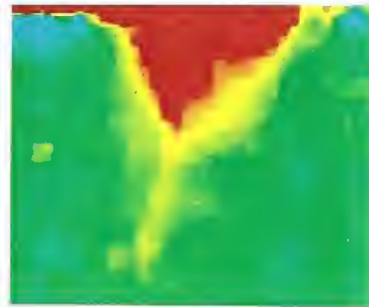
(a)



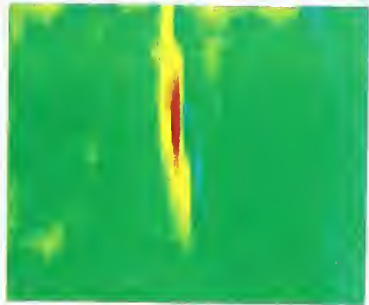
(b)



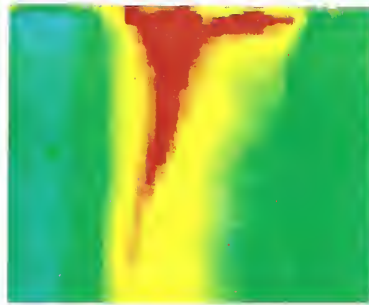
(c)



(d)



(e)



(f)

Figure 7. (a) and (b) are optical micrographs of the damage zone generated by scratching in a fine-grain silicon nitride and a coarse-grain silicon nitride; (c) and (d) are the thermal wave images using the normal deflection component of the probe beam; and (e) and (f) are the thermal wave images using the transverse deflection component of the probe beam. (The scan area for the thermal wave images is $160\ \mu\text{m} \times 170\ \mu\text{m}$).

beam is not sensitive to microcracks that are perpendicular to the surface, while the thermal wave images obtained from the transverse component of the deflected probe beam is not sensitive to microcracks that are parallel to the surface. Therefore, it is important to choose an appropriate imaging mode for the detection of cracks, that may be either parallel or perpendicular to the surface. The third issue is the effect of modulation frequency on heat penetration depth and detection resolution, since a higher frequency results in a better detection resolution, but a smaller detection depth. Therefore, the modulation frequency must be selected to balance the trade-off between the detection depth and the detection resolution.

The thermal wave imaging technique, however, is not suitable for on-line inspection of machined surfaces as it requires a clean environment and an accurate arrangement of the optical system. But, unlike other inspection systems, the thermal wave measurement technique does not require sample immersion in a liquid or the use of a vacuum environment. Therefore, the thermal wave measurement technique can be used for non-destructive evaluation of machining damage for different materials in a laboratory environment.

Appendix 1

“Non-Destructive Detection of Damage Produced by a Sharp Indenter in Ceramics”

Submitted for Publication to

Journal of Engineering Materials and Technology

December 1994

NON-DESTRUCTIVE DETECTION OF DAMAGE PRODUCED BY A SHARP INDENTER IN CERAMICS

Hyo-Sok Ahn¹, Lanhua Wei², and Said Jahanmir
National Institute of Standards and Technology
Gaithersburg, Maryland

ABSTRACT

The feasibility of an ultrasonic technique using normal-incident compressional waves and a thermal wave measurement technique was evaluated for their sensitivity to surface and subsurface damage in ceramics. Well-defined damage in the form of surface and subsurface cracks was introduced by Vickers indentation in soda-lime glass and silicon nitride. The indentation impressions were first examined by optical microscopy to identify the types of cracks and to measure the size of the indents and cracks. As expected, indentation produced median/radial cracks emanating from the indent corners and subsurface lateral cracks. The ultrasonic technique was successful in detecting the subsurface lateral cracks in both materials. The signals obtained by focusing the transducer into the material (i.e., defocusing) was used to estimate the depth of subsurface cracks. The lateral cracks and the median/radial cracks were detected by the thermal wave measurement technique using the optical beam deflection method. The lateral cracks and the median/radial cracks were identified separately by using two deflection components of the probe beam. The transverse deflection component of the probe beam was used for the detection of the median/radial cracks, whereas the normal deflection component was used for the detection of the lateral cracks. The results are discussed in terms of the applicability of these two techniques as on-line non-destructive methods for the detection of machining-induced damage in ceramics.

¹ Guest Scientist on leave from Korea Institute of Science and Technology, Seoul, Korea.

² Guest Scientist on leave from Wayne State University, Detroit, MI 48202.

INTRODUCTION

The demand for advanced ceramic materials, such as silicon nitride and silicon carbide, for use in engineering applications has been growing rapidly. These materials are attractive due to their high strength at elevated temperatures, resistance to chemical degradation, wear resistance, and low density. Although there have been considerable improvements in fabrication and machining of ceramics, surface and subsurface damage induced by machining are still a major problem [Jahanmir, 1993]. A critical form of machining damage that is detrimental to the performance of ceramic components is the microcracks formed on and below the machined surfaces. This form of damage can adversely affect the strength of ceramic components [Koepke and Stokes, 1977; Marshall et al., 1983; Chen et al., 1991; Allor et al. 1993; and Mayer and Fang, 1993]. The thickness of this damage zone ranges from a few micrometers to tens of micrometers depending on the material properties and such machining conditions as material removal rate, grinding wheel speed, and wheel grit size.

The overall goal of this research is to evaluate and compare two non-destructive techniques, namely an ultrasonic method and a thermal wave measurement technique, for the detection of grinding-induced surface and subsurface cracks in ceramics. In the present study, this type of damage is simulated by indentation. Normal loading by sharp indenters, such as Vickers and Knoop diamond pyramidal indenters, produces a permanent impression in the surface and three types of cracks, namely radial, median and lateral cracks, beneath and around the indenter [Lawn, 1993; Cook and Pharr, 1990; and Chandhri and Phillips, 1990]. Figure 1 is a schematic diagram of the cracks typically generated by a sharp indenter under large loads. Radial cracks are generated from the edge of the contact impression (usually at the corner of the indent) perpendicular to the surface. Median cracks are generated beneath the plastic deformation zone and perpendicular to the surface with a circular geometry in the crack plane; these cracks are often referred to as the penny-shaped median cracks [Lawn and Swain, 1975]. The penny-shaped median cracks can further extend upward toward the surface and join with the radial cracks, forming half-penny cracks by additional loading or unloading depending on the material [Chandhri and Phillips, 1990]. The lateral cracks form during unloading below the surface from the microcracks in the plastic zone and propagate parallel to the surface [Hagan and Swain, 1978].

The crack system developed by indentation has been used to formulate a model for wear and abrasive machining, i.e., grinding of brittle ceramic materials [Evans and Marshall, 1981]. According to this model, the material removal process during grinding of brittle ceramics consists of formation and propagation of lateral cracks beneath the contact between the abrasive particles and the surface. A recent

study [Xu and Jahanmir, 1994] has shown that although median and lateral cracks form during single-point scratching of ceramics, the contribution of lateral cracks to the material removal process is negligible under light loads and a limited number of repeated passes. This investigation [Xu and Jahanmir, 1994] has concluded that material removal in grinding of ceramics occurs by formation of microcracks along the grain boundaries leading to grain dislodgement. However, the median and lateral cracks are generated and remain in the material as near-surface damage, especially in fine-grain ceramics.

Marshall et al. [1983] have described the grinding-induced damage as a series of adjoining semi-elliptical median/radial cracks beneath a shallow layer with compressive residual stress. Although the semi-elliptical cracks behave as flaws and would tend to decrease the fracture strength of the component, the compressive stress provides resistance to strength degradation. Nevertheless, depending on the type of machining process and material properties, these microcracks can lead to a reduction in the fracture strength of ceramics [Koepke and Stokes, 1977; Rice, 1993; and Mayer and Fang, 1993]. Since the median/radial cracks are directional, with the crack plane parallel to the machining direction, it has been observed that strength reduction is largely dependent on the orientation of the machining direction with respect to the direction of major tensile stresses in the ceramic part [Rice, 1993; and Strakna et al., 1994]. Therefore, detection of the median/radial cracks is of prime importance in non-destructive evaluation of machined ceramics.

Although substantial effort has been devoted to the development of non-destructive evaluation (NDE) techniques for advanced ceramics, it was not until the early 80's that several NDE techniques such as ultrasonic detection, thermal wave imaging and micro-radiography became available for the detection of micrometer-sized subsurface damage [Rocenswaig et al., 1985; Edwards, 1988; and Friedman et al., 1988]. Ultrasound related techniques have been shown to be highly effective for assessing surface and near-surface damage in ceramics; and in view of their superiority over other techniques [Friedman et al., 1988], they are promising for practical use as in-process monitoring techniques. Several publications have addressed the application of leaky surface wave (i.e., wave propagation parallel to the surface) for the detection of subsurface damage through acoustic microscopy [Yamanaka and Enomoto, 1982; Yamanaka et al., 1985; Lawrence et al., 1990; and Ahn and Achenbach, 1991]. The acoustic microscope offers the ability to image the subsurface features in materials that are opaque to other types of radiation. Using high-frequency transducers, detection of small surface and subsurface flaws, undetectable by conventional ultrasonic methods, is possible by acoustic microscopy. However, the feasibility of using normal-incident compressional waves for detection of surface and subsurface damage has not been

established.

Similar to the ultrasonic techniques, thermal wave methods have been successfully applied to the non-destructive evaluation of ceramic materials [Grice et al., 1983; Inglehart, 1990; and Rantala, 1990]. Thermal waves generated on a sample surface by a periodic heat source, for example a laser beam, propagate into the material to a certain depth depending on the modulation frequency and the thermal properties of the material. Because the temperature profile in the heated region is sensitive to changes in the heat flow in the material, thermal wave techniques can be used for the detection of both surface and subsurface defects acting as heat barriers in the material under investigation. An important advantage of the thermal wave measurement technique over other NDE methods is that the thermal waves are relatively insensitive to the mismatch of the thermal properties of the specimen and the surrounding medium. Therefore, there is no need for immersion of the sample in a special medium, and the measurement can be conducted in air.

In this paper, well-defined surface and subsurface microcracks generated by Vickers indentation in glass and silicon nitride are evaluated by the ultrasonic method using normal-incident compressional waves and by the thermal wave measurement technique using the optical beam deflection method. These two techniques are compared for non-destructive evaluation of indentation damage. The crack system produced by indentation in these materials probably represents a severe form of damage that may be present in machined surfaces. Therefore, analysis of these cracks provides a measure for the sensitivity of the chosen NDE techniques for detection of such damage. In particular, the feasibility of these techniques for the detection of different types of cracks (median/radial versus lateral) in different materials is evaluated and the application of these techniques to the detection of machining damage in ceramics is discussed.

SPECIMEN PREPARATION

Two types of materials were selected for this study. A polished soda-lime glass was selected to provide a reference since the subsurface lateral cracks can be observed in this material using an optical microscope. A hot-isostatically-pressed silicon nitride with a grain size less than 1 μm was selected to represent a high-strength ceramic used in precision bearing applications. The silicon nitride specimen was polished with 1 μm diamond paste to reduce the influence of surface roughness on the measurements.

Two indentations separated by 150 μm were made in the glass specimen with a Vickers indenter under a load of 9.80 N. This separation distance was selected so that the radial/median cracks associated with the indents would connect and form a longer crack. Figure 2 shows an optical reflection micrograph of the glass specimen subjected to a pair of Vickers indents. The diagonal dimension of the indents is approximately 52 μm . Vertical cracks in the form of median/radial half-penny cracks are observed emanating from the corners of the indents, including a prominent segment where they join between the proximate corners of the indent pair. Secondary radial cracks emerging from the edge of the contact impression and propagating into the surrounding material at an angle to the axis of the impression diagonal are also seen. Lateral cracks, by virtue of their subsurface optical reflection, are revealed as bright flares beneath and surrounding the indents. Usually, the lateral cracks form inside the plastic zone near the elastic-plastic boundary [Hagan and Swain, 1978]. Since diameter of the subsurface plastic zone scales with the indentation diagonal, location of the lateral cracks, in this case, can be estimated to be about 26 μm below the surface assuming that the plastic zone is semi-spherical.

Two non-interacting single indentations were made in the silicon nitride specimen at two different loads. A small indent was made with a 7.84 N load to produce an indent without significant cracking in order to evaluate the influence of indent geometry on the ultrasound results. A larger indent was made with a 98.0 N load to produce a well-defined lateral and median/radial crack system. Figure 3 shows the optical micrographs of the Vickers indents at the two loads in silicon nitride. The diagonal lengths of the indents are approximately 30 and 89 μm , respectively. The indentation performed at the lower load has produced a symmetrical Vickers impression without a visible median/radial crack, Fig. 3 (a). However, median/radial cracks are clearly visible at the indent corners for the indentation performed at the larger load, Fig. 3 (b). In this case, the length of the cracks emanating from the corners is approximately 50 μm . Considering the diagonal impression of this indent, the location of the lateral cracks is estimated to be approximately 45 μm below the surface.

ULTRASONIC MEASUREMENTS

In the ultrasonic measurement system used in the present investigation, pulsed acoustic waves were generated by a transducer located above the sample surface and the intensity of the echo signals returned from the surface under examination was measured. Normal-incident compressional waves were used to analyze the surface and near-surface damage produced by indentation. The material subjected to compressional pulse waves undergoes displacement (i.e., movement of atoms) in the direction of wave

propagation, imposing an oscillating pressure perpendicular to the surface. At least two mechanisms pertain wherein the echo amplitude of this wave type may be affected by surface and subsurface damage: (1) an increased material compliance, especially due to shallow horizontal subsurface cracks; and (2) phase interference between surface reflections and subsurface reflections from within the wave penetration depth.

Ultrasonic Measurement System

The ultrasonic system, schematically illustrated in Fig. 4, consists of a broadband pulser/receiver, a gate detector, an oscilloscope, a digital voltmeter, a personal computer, and a computer-controlled 4-axis stage (X, Y, Z, and Φ .) for line and raster scan. The specimens were immersed in a water bath coupling medium through which the pulsed waves travelled to and from the specimen. The transducers were attached to the scanning stage and were used to transmit and receive ultrasonic signals in conjunction with the pulser/receiver unit. The step size of the raster scan was 5 μm in both X and Y directions. Two focused transducers generating short-wave pulses less than 0.1 μs in duration were used in this investigation. Most of the measurements were carried out using a sharp-focused 50 MHz transducer with a spherical lens (focal length of 5.9 mm and f-number of 0.8). The actual operating frequency of this transducer was measured to be 35 MHz. This transducer produced a measured half-amplitude beam width (known as the effective beam width) of 30 to 35 μm in water at room temperature. At this operating frequency, the ultrasonic wavelength in water is 43 μm . In addition to this transducer, a sharp-focused 100 MHz transducer with a spherical lens (focal length of 5 mm and f-number of 0.8) and a 150 MHz transducer (focal length of 2 mm and f-number of 1.33) were used for the silicon nitride specimen. The 100 MHz transducer had a measured operating frequency of 75 MHz and a half-amplitude beam width of 20 μm .

The peak amplitude voltage from the reflected ultrasonic signals were acquired by the gated peak detector when a selected area of specimen was scanned. The peak amplitude data (in mV) were then read and recorded by a personal computer through an analog to digital converter board. The data were plotted using commercial graphics software to analyze the results.

Detection of Surface and Subsurface Damage

The result of an ultrasound raster scan for the upper indent in glass, using normal-incident waves, is shown in Fig. 5 as an echo-amplitude contour plot. The tightly contoured region in the center, where

the ultrasonic reflection is dominated by the indent geometry, defines the location of the upper indent. The geometry of the indent and the vertical cracks is superimposed on the contour plot. A comparison between the contour plot in Fig. 5 and the optical micrograph in Fig. 2 reveals a correlation between the shape of the lateral cracks and the echo-amplitude contour shape and size. Our interest for the detection of subsurface damage is in the immediate region surrounding the indent, where a reduction in echo-amplitude by about 15% relative to the undamaged background level is observed. This reduction in echo-amplitude is a result of an increased material compliance by the reflected compressional waves due to the presence of lateral cracks beneath the indent surface. It is noted from Fig. 5 that the vertical cracks, with their planes parallel to the incident compressional waves, are not discernible. Detection of vertical cracks would require surface-propagating leaky waves traveling perpendicular to the crack planes.

The results for ultrasonic examination of the small indent in silicon nitride are shown in Fig. 6 (a), where the indent shape is superimposed on the contour plot of the echo-amplitude. Dense contours, similar to the results obtained on the glass sample, are observed in the region of the indent. The circular band of amplitude reduction around the indent may be associated with the impression and/or the plastic deformation region beneath and around the indent. The reduction of the echo-amplitude is more clearly represented in the 3-D plot of Fig. 7 (a). The width of the circular band of amplitude reduction surrounding the indent is approximately $15 \sim 20 \mu\text{m}$, which corresponds to the beam width or the lateral resolution of the ultrasonic beam for the 50 MHz transducer used for obtaining the signal. Another measurement with a 150 MHz transducer showed a similar result supporting this observation. Therefore, the circular pattern in the contour plot of Fig. 6 (a) is believed to be associated only with the indent impression, and is not significantly influenced by the plastic deformation region surrounding the indent.

The results of the ultrasonic measurements on the larger indent in the 3-D plot of the echo-amplitude map in Fig. 7 (b) demonstrates a conspicuous region of amplitude drop. The contour plots in Figs. 6 (b) and (c) taken with the 50 MHz and the 100 MHz transducers clearly demonstrate that the contours are not circular, but are distorted. The diamond-marks superimposed on the contour plots delineate the size and shape of the indents and their probable location, as well as the length of the median/radial cracks emanating from the indent corners. There is a close correlation between the location of the median/radial cracks and the distortion of the contours. It is not clear whether this distortion is caused by the vertical cracks or by the lateral cracks below the surface. Since compressional waves are not sensitive to vertical cracks, it can be surmised that the contour shape is either influenced by the lateral cracks or by weak interference effects from the vertical cracks.

In an attempt to increase the sensitivity of ultrasonic pulses to such subsurface structures as lateral cracks and to obtain an estimate for the location of subsurface cracks, the transducer was focused below the surface. This is often referred to as defocusing and it is accomplished by reducing the distance between the transducer and the specimen surface. Figure 8 shows the echo-amplitude line scans over the center of the large indent in silicon nitride at various depths of focus Z . The results in Fig. 8 (a) and (b) were obtained with the 50 MHz and 100 MHz transducers, respectively. In Fig. 8 (a), the topographical influence of the indent impression is observed as a large decrease in the echo-amplitude when the transducer is focused on the surface. A substantial drop in the echo-amplitude is also observed for the signal obtained at a depth of 13 μm . When the transducer is focused to a depth of 25 μm , the drop in the echo-amplitude becomes less, and the magnitude of the echo-amplitude in the indent region increases above the values obtained at 13 μm . This trend continues when the transducer is focused to greater depths, and the drop in the echo-amplitude becomes negligible at a depth of 50 μm . A similar trend is observed in Fig. 8 (b) for the 100 MHz transducer, where the drop in echo-amplitude is negligible at $Z = 60 \mu\text{m}$. These results suggest that the lateral cracks are located about 50-60 μm below the surface. This value agrees with the estimate obtained based on the size of the indentation impression.

THERMAL WAVE MEASUREMENTS

The thermal wave measurement technique is a powerful tool for evaluating the thermal properties of materials. This technique is based on the measurement of temperature distribution (both in time and in space) generated by localized heating of the material being investigated. The thermal wave technique used in this work is based on the optical beam deflection method (also called the "mirage effect method") [Boccara et al., 1980]. In this technique, the specimen is locally heated by a modulated laser beam. This modulated heating generates a changing temperature distribution, i.e. thermal waves, in the specimen. The thermal waves returning from the sample cause a modulated change in the index of refraction of the air above the surface. The temperature distribution in air is then detected by measuring the deflection of a laser probe beam passing through the air in a close proximity to the sample surface. This method is, in principle, sufficiently sensitive for the detection of surface and near-surface microcracks, since microcracks in a material change the local heat flux.

Thermal Wave Measurement System

A schematic diagram of the experimental setup is shown in Fig. 9. An argon-ion laser beam is chopped by an acousto-optic modulator at a certain frequency and is focused on the sample surface to provide a localized periodic heat source. A He-Ne laser probe beam is directed at a near-grazing angle to the surface, and is refracted by the time varying gradient in the index of refraction of the air. The magnitude and phase of the deflected probe beam (represented as a vector) is measured by a position-sensitive quad-cell detector. The output voltage is amplified and fed into two separate vector lock-in amplifiers: one to monitor the vector component normal to the surface, i.e., the normal deflection; the other to monitor the vector component parallel to the surface, i.e., the transverse deflection.

In the measurements of the indented specimens, the $1/e$ -radius of the heating beam was $10\text{ }\mu\text{m}$ and that of the probe beam was $15\text{ }\mu\text{m}$. An X-Y stage, controlled by a personal computer, was used to scan the specimen surface in order to obtain a thermal wave image of an area under investigation. Step sizes of 5 and $10\text{ }\mu\text{m}$ were used for the glass and silicon nitride samples, respectively. The voltage signals obtained from the lock-in amplifiers were converted to digital data and were plotted using a commercial graphics software. In the received image, the background signal level from the material was distinguished from the peak signal level caused by a local temperature rise due to the reflection of thermal waves from a heat barrier, namely a crack or other types of defects.

Detection of Surface and Subsurface Damage

The transverse component of the deflected probe beam (parallel to the sample surface) was used for the detection of the median/radial cracks emanating from the corners of the indent in glass. The transverse component is sensitive to the thermal waves with preferential propagation along the surface [Grice et al., 1983] and perpendicular to the vertical crack plane. An image of a raster scan on the glass specimen is shown in Fig. 10 (a), using a step size of $5\text{ }\mu\text{m}$ in both X and Y directions. The scan covers a $200 \times 200\text{ }\mu\text{m}$ area, giving approximately the same scale as the schematic in Fig. 10 (b). The modulation frequency used was 20 Hz , corresponding to the thermal diffusion length of $100\text{ }\mu\text{m}$ in the material. In the image, the darker areas indicate a larger signal, corresponding to higher local temperatures on the specimen. In these high temperature regions, the heat flow is disturbed by the existence of a defect or a crack. The two secondary radial cracks and the median/radial crack in the Y direction can be clearly seen in Fig. 10 (a) as a "Y". However, the other median/radial cracks located along the X direction are not observed, because these cracks are located in a plane parallel to the heat

propagation direction and do not disturb the heat flow. The lateral cracks and the indent impression can be only vaguely seen in the background of the thermal wave image in Fig. 10 (a). In order to detect the lateral cracks, the normal deflection component of the probe beam must be used.

A thermal image of the large indent on the silicon nitride sample, using a step size of $10\text{ }\mu\text{m}$ and the normal component of the deflected probe beam, is shown in Fig.11 (a). The bright spot located in the middle of the image corresponds to the center point of the indent; the surrounding area with different grey scale indicates reflection of the thermal waves from subsurface damage, i.e., the lateral cracks. The vertical cracks are not clearly seen in this image because the normal component of the deflected beam is more sensitive to cracks that are parallel to the surface. Figure 11 (b) is a schematic drawing of the indentation damage on the silicon nitride specimen showing the indent and a well-developed median/radial crack system. Figure 11 (c) is a thermal image using the transverse component of the deflected probe beam, showing only the median/radial cracks that are perpendicular to the scan direction, i.e., parallel to the Y-axis. Similar to the results obtained on the glass sample, the median/radial crack located along the X direction is not detected.

The length of the median/radial crack detected by the thermal wave measurement technique, Fig. 11 (c), is approximately $240\text{ }\mu\text{m}$, which is about 20% larger than the length measured in the optical microscope. This discrepancy, also observed by Rantala et al. [1990], may be related to the crack opening, since tightly closed cracks cannot be observed by optical microscopy. As a confirmation of this point, the signal from the median/radial crack located on the top corner of the indent is shown in the 3-D plot in Fig. 12. The figure indicates that the signal amplitude decreases as the distance from the indent corner is increased. This behavior may be associated with the decrease in the crack opening along the crack.

DISCUSSION

In the present study, we utilized an ultrasonic technique and a thermal wave measurement technique to analyze the indentation damage in glass and silicon nitride. Based on the assumption that indentation damage is similar to the damage generated by grinding [Evans and Marshall, 1981; Marshall et al. 1983; and Rice, 1993], detection of indentation damage can be used to establish the feasibility of these techniques for detecting machining damage. The vertical semi-elliptical cracks, often associated with machining damage in ceramics [Rice, 1993], can be regarded as the half-penny median cracks in Vickers indentation. These cracks were not clearly distinguished from the lateral cracks by the ultrasonic

technique used in the present study. Therefore, the normal-incident compressional ultrasonic waves cannot be used for the detection of vertical cracks. However, this technique is capable of detecting subsurface lateral cracks. Although the influence of lateral cracks on the fracture strength of ceramic components is not as severe as vertical cracks, their role must not be neglected when the surface of a component is subjected to contact loads, for example in bearings, where subsurface lateral cracks may result in premature failure.

The vertical cracks can be more effectively observed with an acoustic microscope by monitoring the leaky Rayleigh waves than by the compressional waves used in this study. However, application of acoustic microscopy as an on-line inspection system is problematic, since it generally requires high frequencies in GHz range for the detection of micrometer-sized cracks [Yamanaka and Enomoto, 1982; Yamanak et al., 1987 and 1983; and Lawrence et al., 1990]. A particular advantage of the ultrasound technique used in the present study is its application to on-line machining, where the cutting fluid can be used as the coupling medium to bridge the ultrasonic waves between the transducer and the specimen [Blessing and Eitzen, 1989].

The thermal wave measurement technique was shown to be a reliable method for the detection of both surface and subsurface cracks produced by indentation. Although the feasibility of this technique has been shown by Grice et al. [1983], Inglehart [1984], and Rantala et al. [1990] for detecting lateral and median/radial cracks in silicon carbide and silicon nitride ceramics, separation of the signals produced by each crack type was not considered in those studies. In the present study, it was shown that by separating the two deflection components of the probe beam, the two types of cracks, i.e., median/radial and lateral, can be distinguished. This separation provides a unique approach in the analysis of cracks, and possibly other types of damage that may be produced by machining. In addition, glass and silicon nitride with two orders of magnitude difference in thermal diffusivity (from a thermal insulator to a thermal conductor) were examined in the present study, confirming the feasibility of thermal wave measurement technique for use on a wide range of materials. The present study also showed that vertical cracks with their planes parallel to the scan direction are not detected by the tangential deflection component of the probe beam. This feature can be used to detect anisotropic thermal property change, for example orientation of cracks.

The thermal wave imaging technique, however, is less applicable as an on-line inspection system than the ultrasonic technique using the normal-incident compressional waves, because the former requires a clean environment and an accurate arrangement of the optical system. On the other hand, by not

requiring sample immersion in a liquid, the thermal wave technique is more flexible in handling different types of materials that could react with water. At the present, the thermal wave measurement technique is an excellent non-destructive evaluation method for sample analysis in a laboratory environment.

In this paper we have focused our attention on the analysis of relatively large cracks produced by indentation. It should be recognized that the type of damage introduced by indentation may represent an upper limit to the damage produced in machining. Therefore, the sensitivity of the ultrasonic and the thermal wave measurement techniques to smaller cracks must be evaluated further. For example, subsurface microcracks formed along the grain boundaries in machining [Xu and Jahanmir, 1994] could influence the service life of components subjected to wear and corrosion. Therefore, detection of all three types of machining-induced cracks, i.e., median/radial, lateral, and grain boundary microcracks, is important to ensure a reliable service.

CONCLUSIONS

- (1) The ultrasonic technique using normal-incident compressional waves was able to detect subsurface lateral cracks associated with indentations in silicon nitride and soda lime glass.
- (2) Focusing the transducer into the material provided an estimate for the depth of subsurface cracks.
- (3) The thermal wave measurement technique using the optical beam deflection method was able to detect both the median/radial and lateral cracks in ceramics.
- (4) By using the two different deflection components of the probe beam in the thermal wave measurement technique, the median/radial cracks and the lateral cracks were separately identified.
- (5) When the transverse deflection component of the probe beam was used in the thermal wave imaging to detect vertical cracks, the cracks along the probe beam scan direction were not detected.

ACKNOWLEDGEMENTS

The authors are grateful to G. V. Blessing for helpful discussions on ultrasonic measurement techniques and for making the ultrasonic measurement system available for this study. The assistance of J. A. Slotwinski in ultrasonic measurements and discussions with G. S. White in thermal wave measurement are gratefully acknowledged. This project was sponsored in part by the U.S. Department of Energy, through the Ceramic Technology Project at the Oak Ridge National Laboratory, and by the Korea Institute of Science and Technology.

REFERENCES

- Ahn, V. S. and Achenbach, J. D., 1991, "Response of Line Focus Acoustic Microscope to Specimen Containing a Subsurface Crack," Ultrasonics, Vol. 29, pp. 482-489.
- Allor, R. L., Whalen, T. J., Baer, J. R., and Kumar, K. V., 1993, "Machining of Silicon Nitride: Experimental Determination of Process/Property Relationships," Machining of Advanced Materials, S. Jahanmir (Ed.), Proceedings of the International Conference on Machining of Advanced Materials, Gaithersburg, MD, July 20-22, 1993, NIST Special Publication 847, National Institute of Standards and Technology, Government Printing Office, Washington, DC, pp. 223-235.
- Blessing, G. V., and Eitzen, D. G., 1989, "Ultrasonic Sensor for Measuring Surface Roughness," Proceedings of Surface Measurements and Characterization, J. M. Bennett (Ed.) SPIE, Vol. 1009, pp. 281-289.
- Boccara, A. C., Fournier, D., and Badoz, J., 1980, "Thermo-optical Spectroscopy: Detection by the 'Mirage effect'," Appl. Phys. Lett., Vol. 36, pp. 130-132.
- Chandhri, M. M., and Phillips, M. A., 1990, "Quasi-static Indentation Cracking of Thermally Tempered Soda-lime Glass with Spherical and Vickers Indenters," Philosophical Magazine, Vol. 62, pp. 1-27.
- Chen, C., Sakai, S., and Inasaki, I., 1991, "Lapping of Advanced Ceramics," Materials & Manufacturing Processes, Vol. 6, pp. 211-226.
- Cook, R. F. and Pharr, G. M., 1990, "Direct Observation and Analysis of Indentation Cracking in Glasses and Ceramics," J. Am. Ceram. Soc., Vol. 73, pp. 787-817.
- Edwards, G. R., 1989, "Non-Destructive Testing of Engineering Ceramics," British Ceram. Trans. J., Vol. 88, pp. 117-123.
- Evans, A. G., and Marshall, D. B., 1981, "Wear Mechanisms in Ceramics," Fundamentals of Friction and Wear of Materials, D. A. Rigney (Ed.), American Society for Metals, Metals Park, OH, pp. 439-452.
- Friedman, W. D., Bhagat, A. R., Srinivasan, M., and Wilson, J., 1988, "An Assessment of Various Methods Which Detect Critical Surface Flaws in Sintered SiC," Review of Progress of Quantitative Nondestructive Evaluation, D.O. Thompson and D.E. Chimenti (Eds.), Vol. 5B, pp. 1509-1518.
- Grice, K. R., Inglehart, L. J., Favro, L., Kuo, P. K., and Thomas, R. L., 1983, "Thermal Wave Imaging of Closed Cracks in Opaque Solids," J. Appl. Phys., Vol. 54, pp. 6245-6255.

Inglehart, L. J., 1984, "Optical Beam Deflection Detection of Thermal Waves in Opaque Solids," Ph. D. Dissertation, Wayne State University, Detroit, MI.

Inglehart, L. J., 1990, "Photothermal Characterization of Creep Damage in SiC-SiO₂," J. Appl. Phys., Vol. 68, pp. 2992-2996.

Jahanmir, S., 1993, Machining of Advanced Materials, Proceedings of the International Conference on Machining of Advanced Materials, Gaithersburg, MD, July 20-22, 1993, NIST Special Publication 847, National Institute of Standards and Technology, Government Printing Office, Washington, DC.

Hagan, J. T., and Swain, M. V., 1978, "The Origin of Median and Lateral Cracks Around Plastic Indents in Brittle Materials," J. Appl. Phys., Vol. 11, pp. 2091-2102.

Koepeke, B. G., and Stokes, R. J., 1977, "Grinding Damage in Ceramics," Society of Manufacturing Eng. Tech. Paper, EM77-358.

Lawn, B. R., 1993, Fracture of Brittle Solids, (2nd ed.), Cambridge University Press, Cambridge, U.K.

Lawn, B. R., and Swain, M. V., 1975, "Microfracture Beneath Point Indentations in Brittle Solids," J. Material Sci., Vol.10, pp.113-122.

Lawrence, C. W., Scruby, C. B., Briggs, G. A. D., and Dunhill, A., 1990, "Crack Detection in Silicon Nitride by Acoustic Microscopy," NDT Int., Vol. 23, pp. 3-8.

Marshall, D. B., Evans, A. G., Khuri Yakub, B. T., Tien, J. W., and Kino, G. S., 1983, "The Nature of Machining Damage in Brittle Materials," Proc. R. Soc. Lond., Vol. A 385, pp. 461-475.

Mayer, J. E., Jr., and Fang, G. P., 1993, "Diamond Grinding of Silicon Nitride Ceramics," Machining of Advanced Materials, S. Jahanmir (Ed.), Proceedings of the International Conference on Machining of Advanced Materials, Gaithersburg, MD, July 20-22, 1993, NIST Special Publication 847, National Institute of Standards and Technology, Government Printing Office, Washington, DC, pp. 205-222.

Rantala, J., Hartikainen, J., and Jaarinen, J., 1990, "Photothermal Determination of Vertical Crack Lengths in Silicon Nitride," Appl. Phys., A 50, pp. 465-471.

Rice, R. W., 1993, "Effects of Ceramic Microstructural Character on Machining Direction - Strength Anisotropy," Machining of Advanced Materials, S. Jahanmir (Ed.), Proceedings of the International Conference on Machining of Advanced Materials, Gaithersburg, MD, July 20-22, 1993, NIST Special Publication 847, National Institute of Standards and Technology, Government Printing Office, Washington, DC, pp. 185-204.

Rocenswaig, A., Opsal, J., Smith, W. L., and Willenburg, D. L., 1985, "Detection of Thermal Waves Through Optical Reflectance," Appl. Phys. Lett., Vol. 46, pp. 1013-1015.

Strakna, T. J, Jahanmir, S., Allor, R. L., and Kumar, K. V., 1994, "Influence of Grinding Direction on Fracture Strength of Silicon Nitride," manuscript in preparation.

Wei, L., 1992, "Thermal Property Characterization of Single Crystal Diamond with Varying Isotopic Composition," Ph. D. Dissertation, Wayne State University, Detroit, MI.

Xu, H. H. K., and Jahanmir, S., 1994, "Simple Technique for Observing Subsurface Damage in Machining of Ceramics," J. Am. Ceram. Soc., Vol. 77, pp. 1388-1390.

Xu, H. H. K., and Jahanmir, S., 1994, "Microfracture and Material Removal in Scratching of Alumina," manuscript submitted to J. of Materials Sci.

Yamanaka, K., and Enomoto, Y., 1982, "Observation of Surface Cracks with Scanning Acoustic Microscope," J. Appl. Phys., Vol. 53, pp. 846-850.

Yamanaka, K., Enomoto, Y., and Tsuya Y., 1985, "Acoustic Microscopy of Ceramic Surfaces," IEEE Trans. Sonics and Ultrasonics, Vol. SU-32, pp. 313-319.

Yamanaka, K., Enomoto, Y., and Tsuya Y., 1983, "Application of Scanning Acoustic Microscope to the Study of Fracture and Wear," Acoustical Imaging, E. Ash and C. Hills (Eds.), Plenum, New York, NY, Vol. 12, pp. 79-87.

Yamanaka, M., Haraguchi, S., and Y. Tsuya, 1987, "Evaluation of Machined Ceramic Surfaces by Using Quantitative Acoustic Microscopy," IEEE Ultrasonics Symposium Proceedings, B. R. McAvoy (Ed.), Denver, CO, October 14-16, 1987, Vol. 1, pp. 591-595.

Figure Captions

- Figure 1. Schematic diagram of cracks generated by indentation of brittle materials with a sharp indenter.
- Figure 2. Optical reflection micrograph showing the two Vickers indents and the associated median/radial and lateral cracks in the glass specimen.
- Figure 3. Optical micrographs of Vickers indents in silicon nitride: (a) 7.84 N load, and (b) 98.0 N load.
- Figure 4. Schematic diagram of the ultrasonic measurement system.
- Figure 5. Ultrasonic echo-amplitude contour plot of the upper indent, using a 50 MHz transducer.
- Figure 6. Echo-amplitude contour plots of the Vickers indents in silicon nitride: (a) small indent examined with a 50 MHz transducer, (b) large indent with cracks examined with a 50 MHz transducer, and (c) large indent examined with a 100 MHz transducer.
- Figure 7. 3-D echo-amplitude maps of the Vickers indents in silicon nitride examined with a 50 MHz transducer: (a) small indent, and (b) large indent with cracks. (The echo-amplitude values are larger in (a) because of a larger amplification factor used during data acquisition.)
- Figure 8. Echo-amplitude results of line scans passing near the center of the large indent in silicon nitride at various depth of focus: (a) with a 50 MHz transducer, and (b) with a 100 MHz transducer.
- Figure 9. Block diagram of the thermal wave measurement system with the optical beam deflection technique [Wei, 1992].
- Figure 10. (a) Thermal wave image of the surface using the transverse deflection component of the probe beam (the scan area is $200 \times 200 \mu\text{m}$) and (b) Schematic drawing of the upper indentation mark with the median/radial cracks in glass.
- Figure 11. (a) Thermal wave image of the large indent on silicon nitride using the normal deflection component of the probe beam, (b) schematic drawing of the indent, and (c) thermal wave image of the same area using the transverse deflection component (the scan area for both images in (a) and (c) is $300 \times 300 \mu\text{m}$).
- Figure 12. 3-D plot of the mirage signal associated with the median/radial crack located in the upper corner of the indent in Fig. 11 (b).

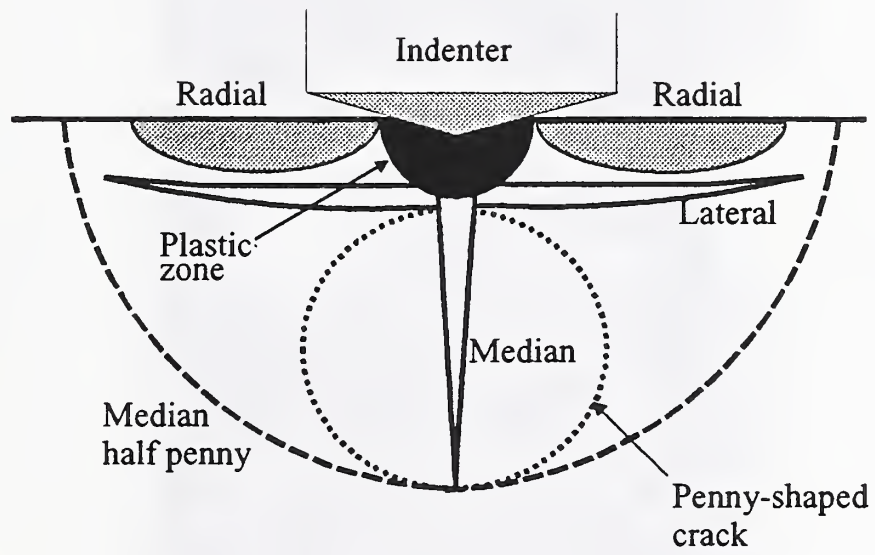


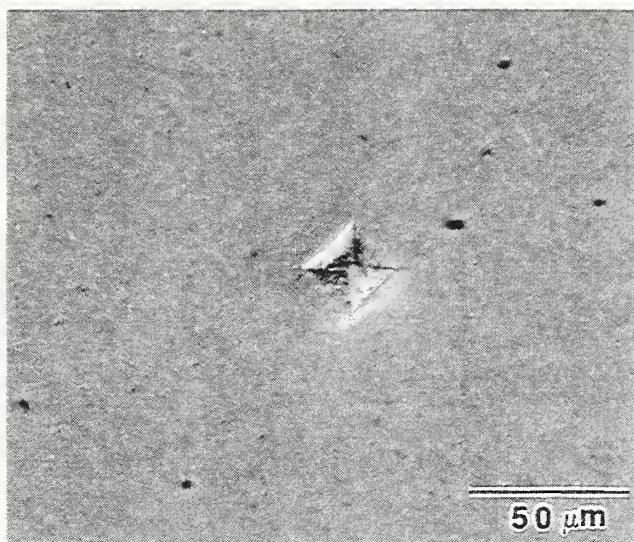
Fig. 1



50 μm

Fig. 2

(a)



(b)

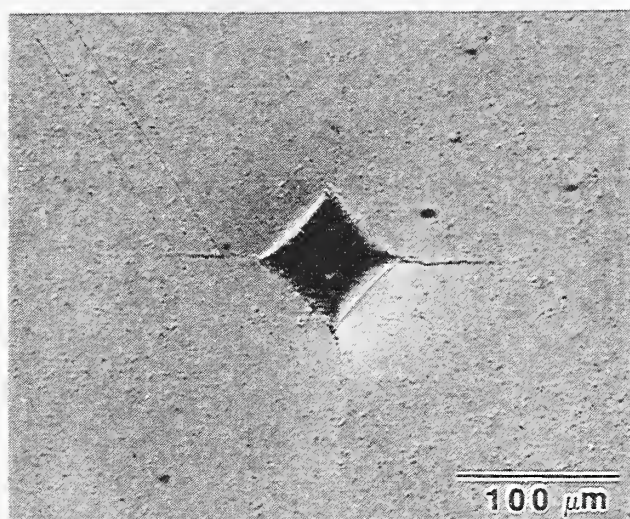


Fig. 3

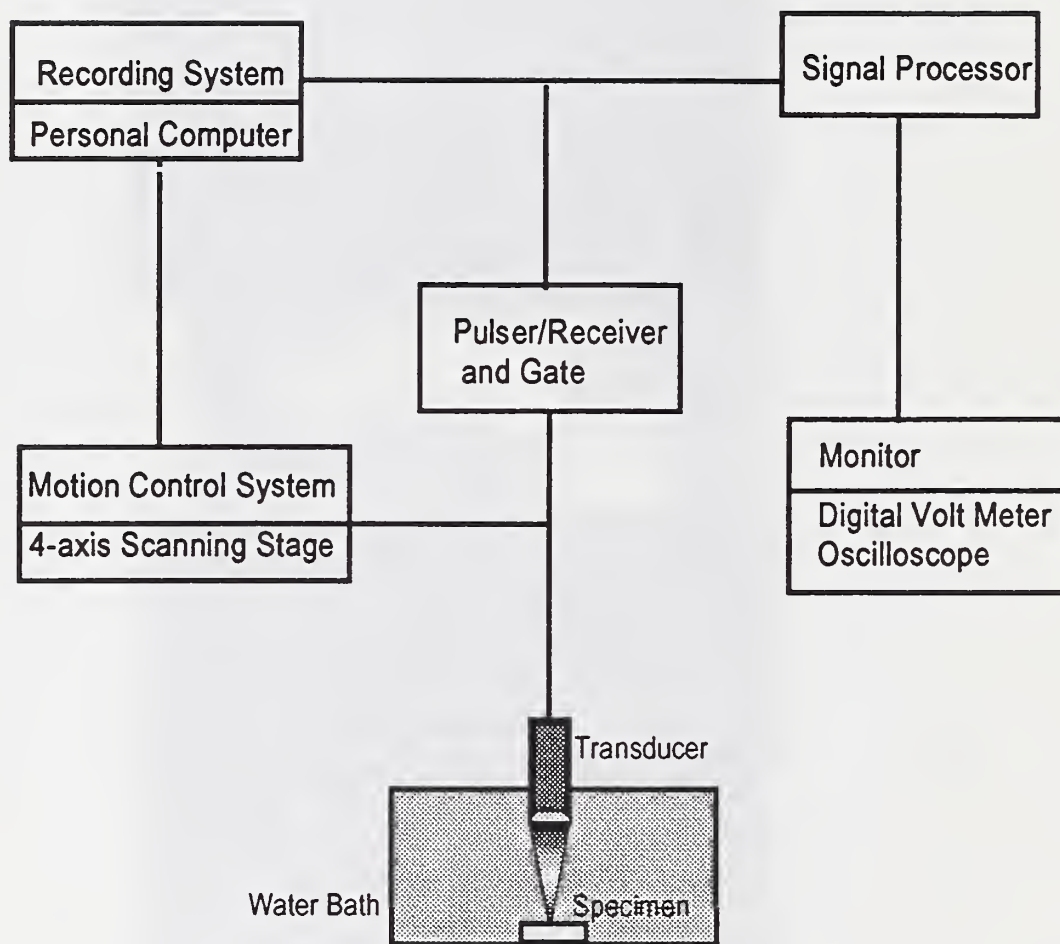


Fig. 4

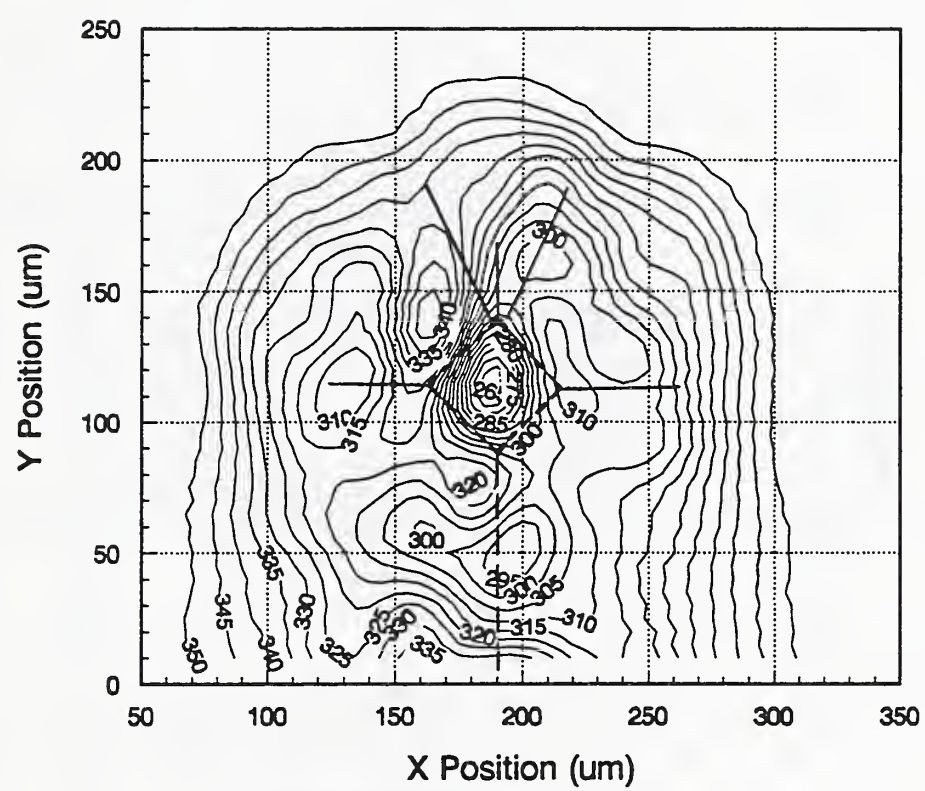


Fig.5

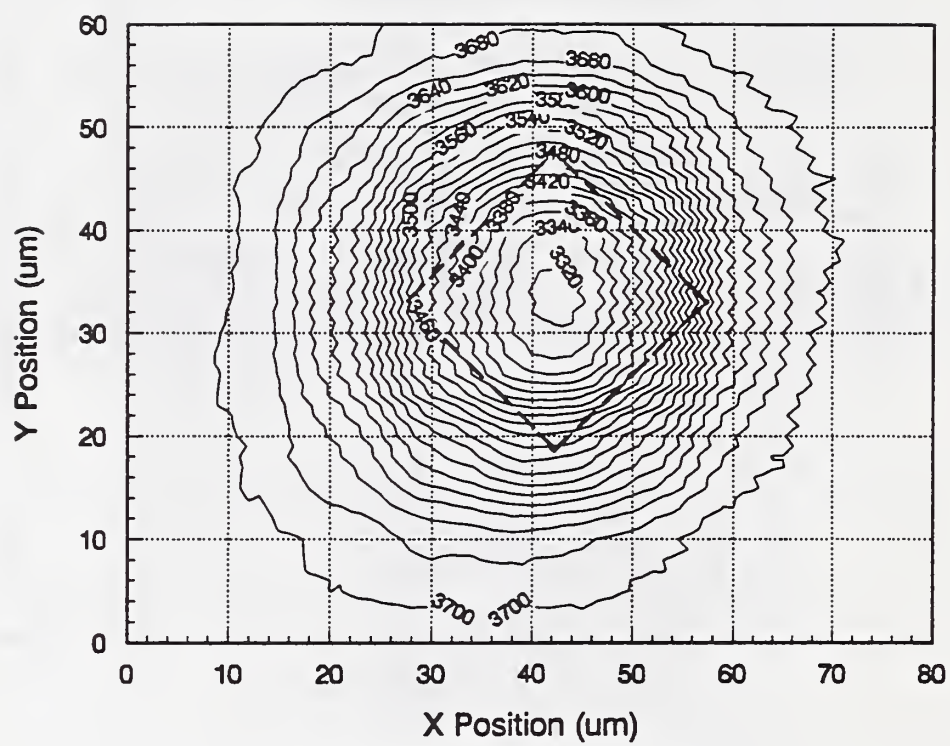


Fig. 6 (a)

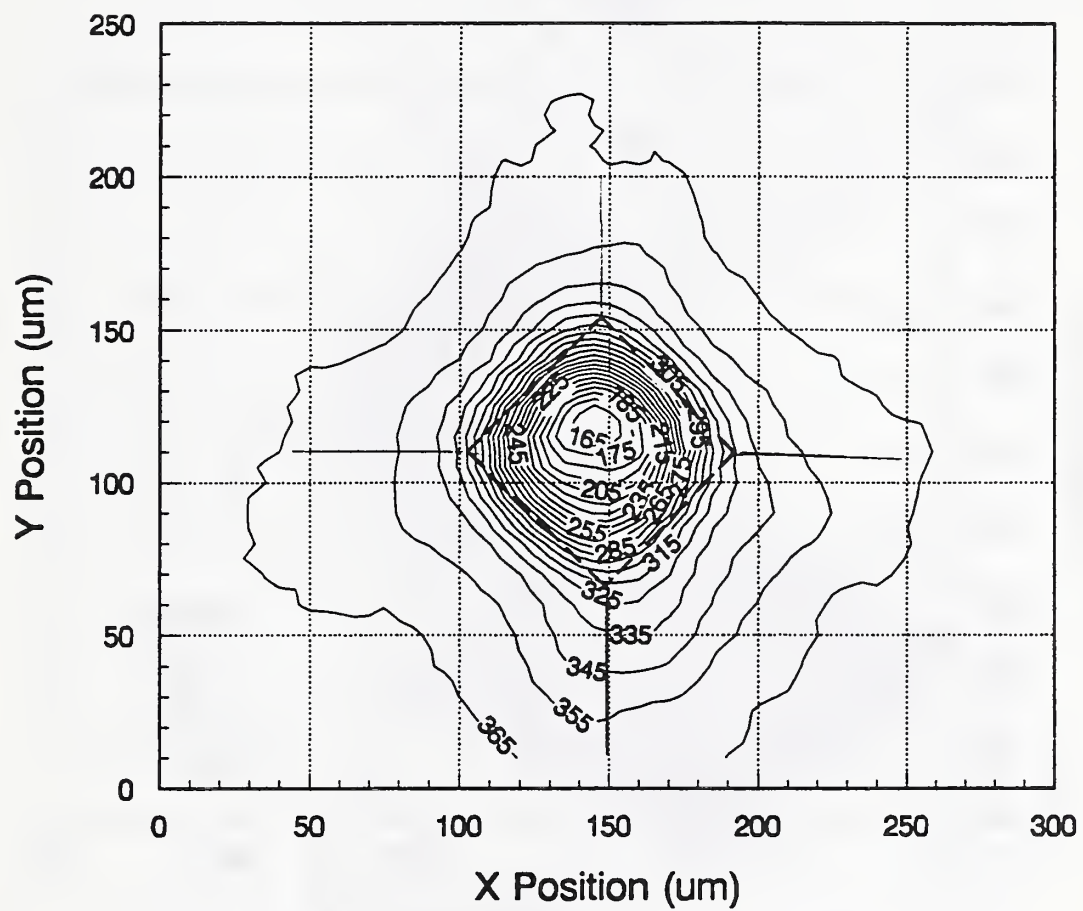


Fig. 6 (b)

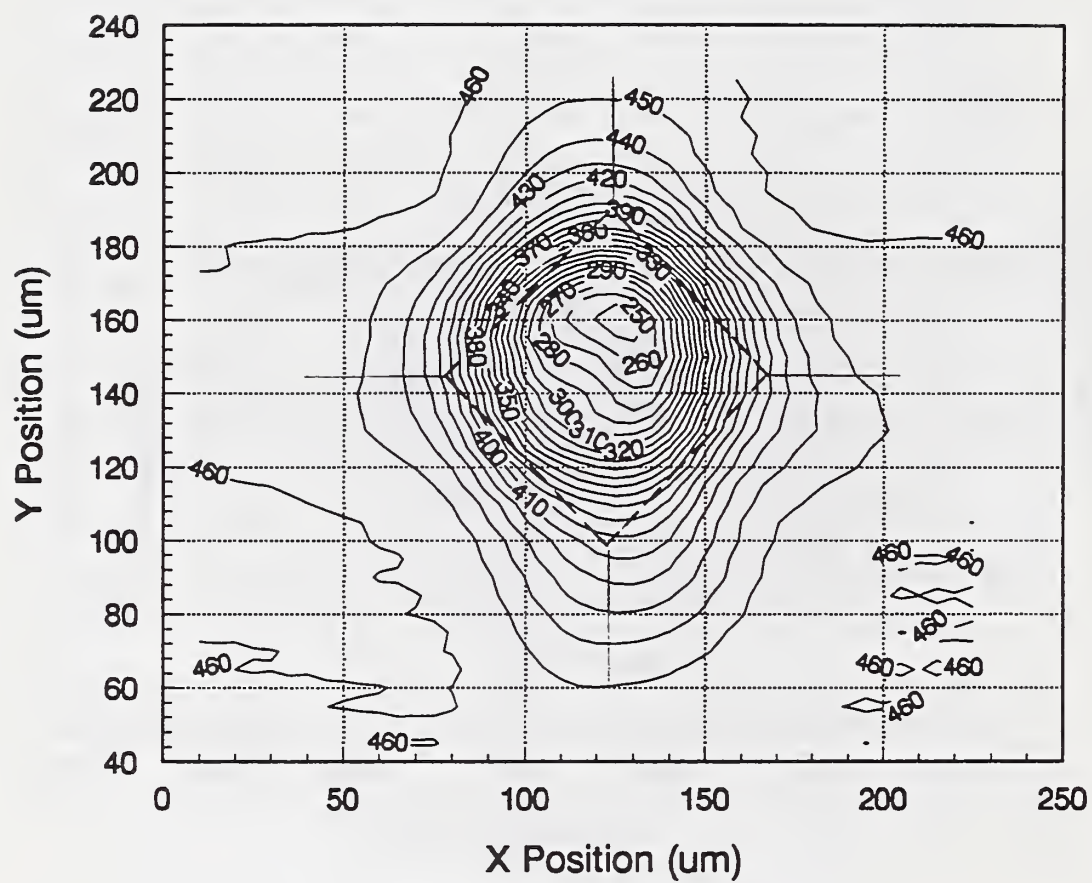
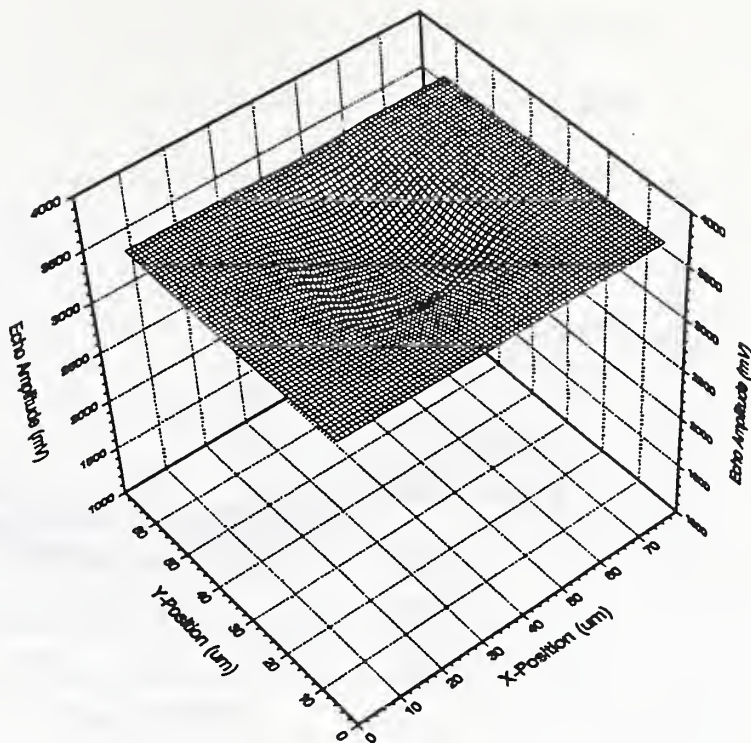


Fig. 6 (c)

(a)



(b)

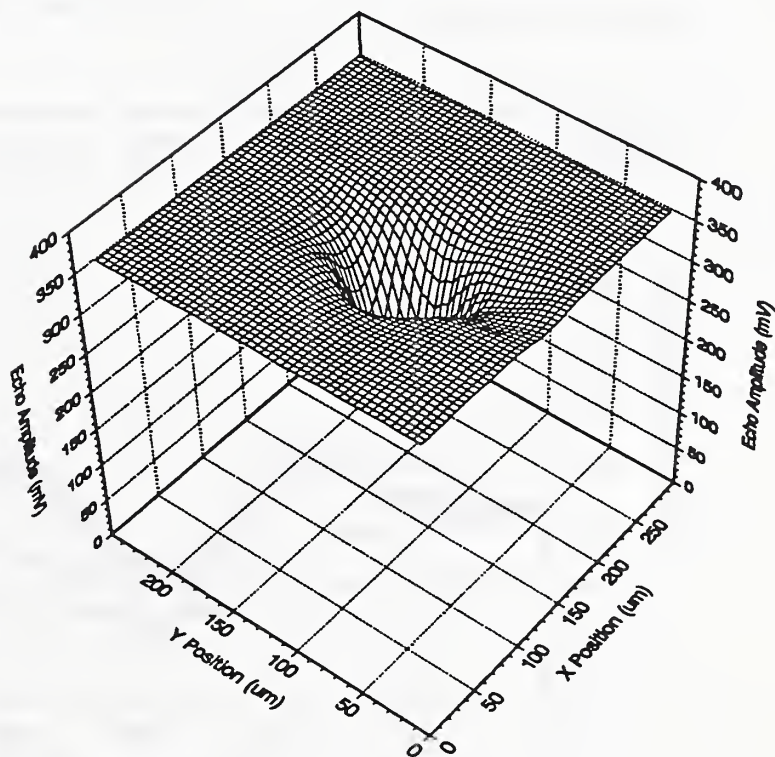


Fig. 7

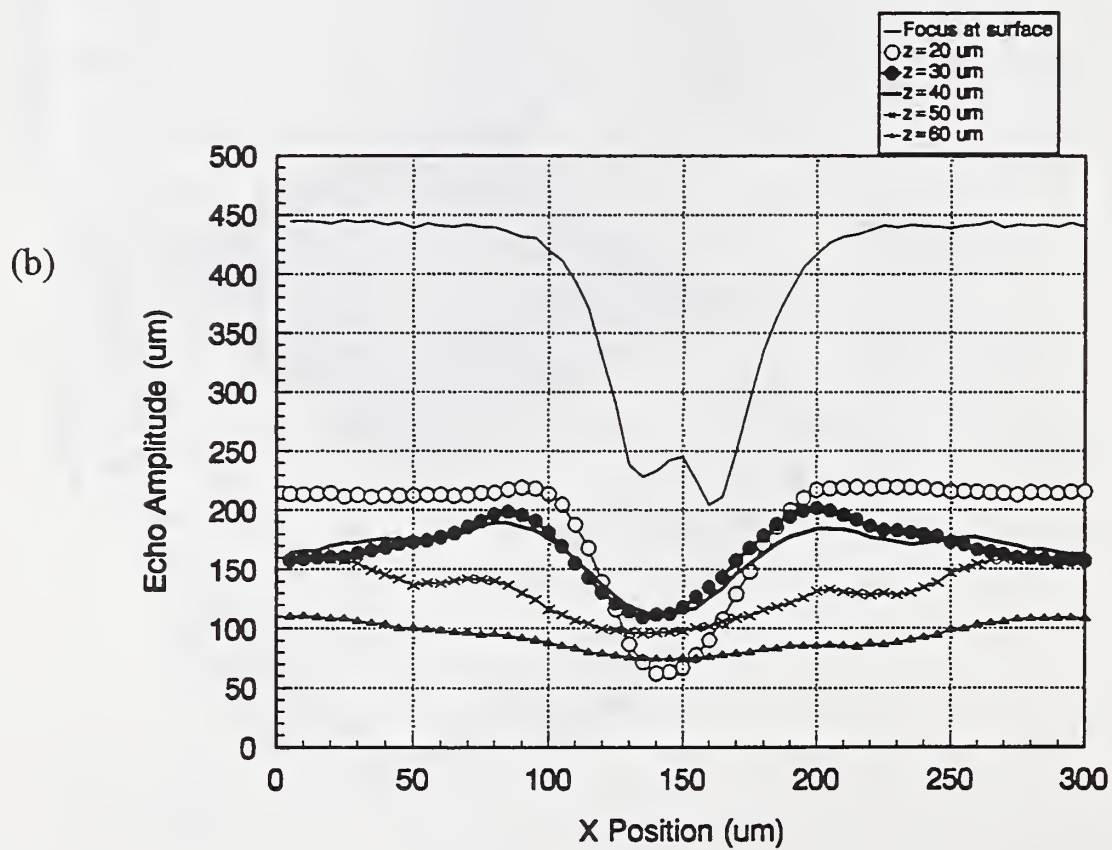
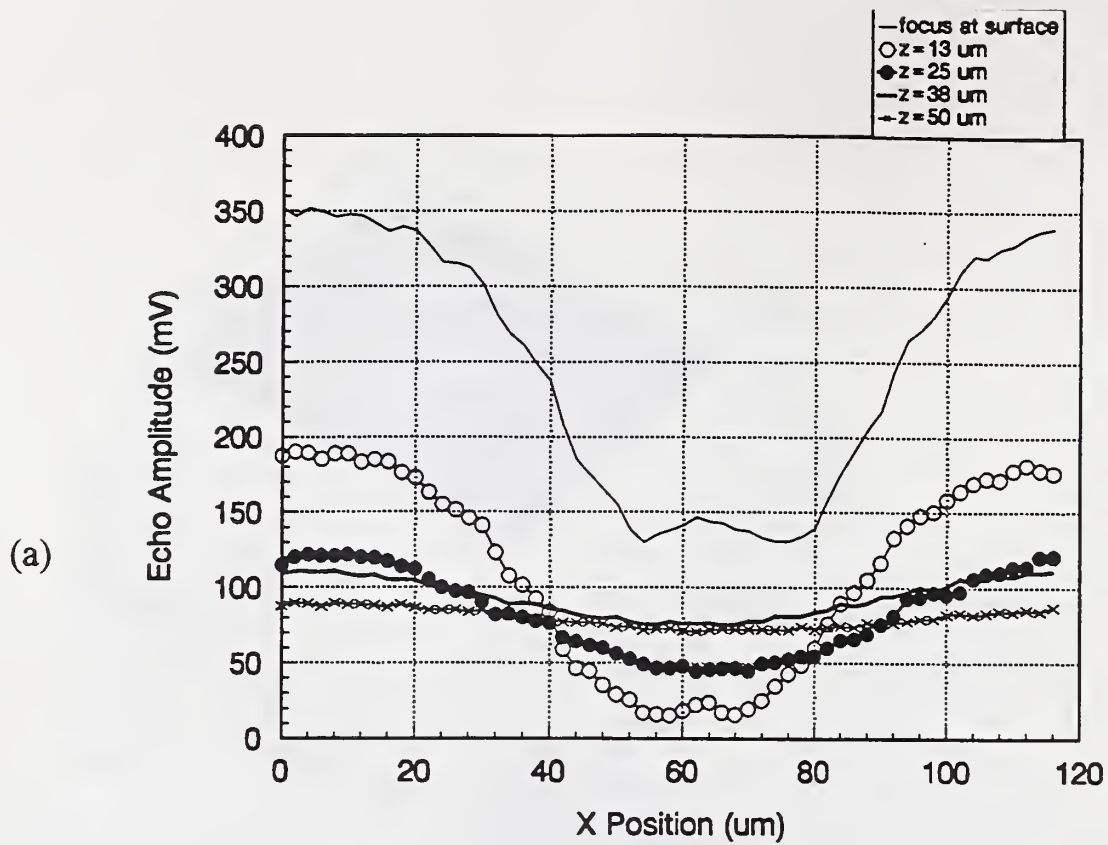


Fig. 8

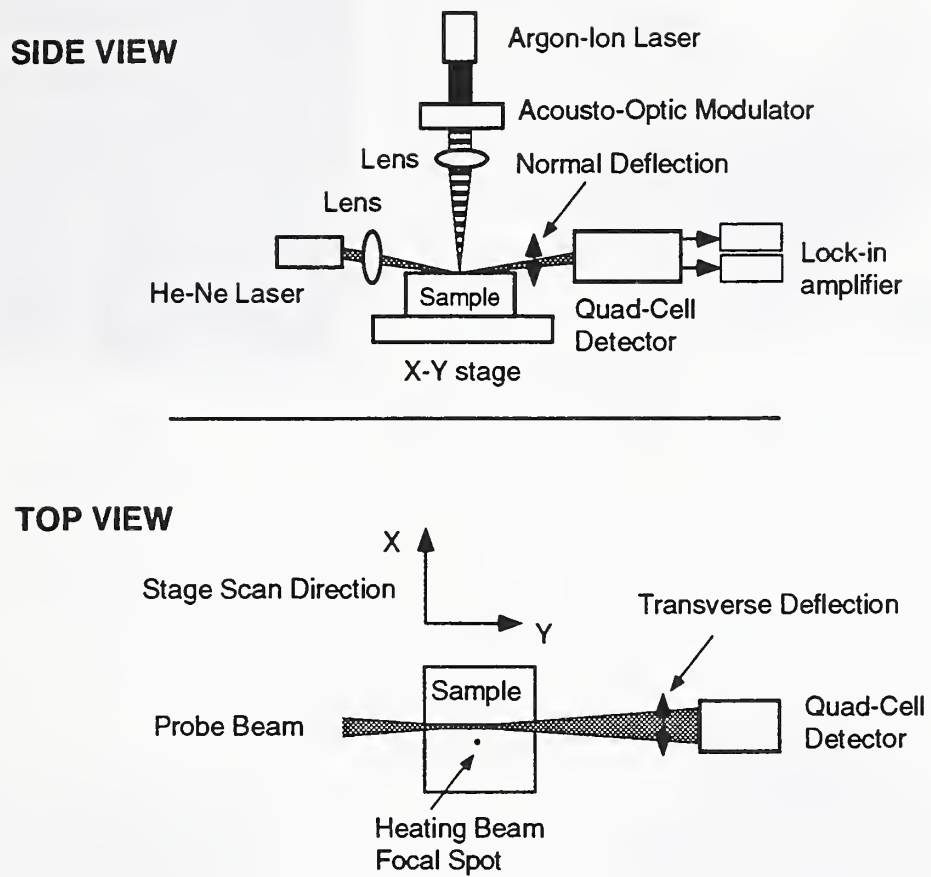


Fig. 9

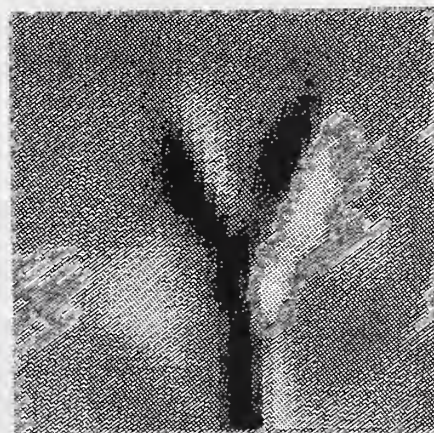
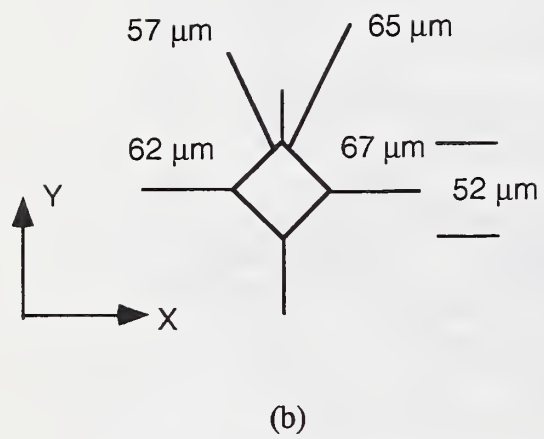


Fig. 10

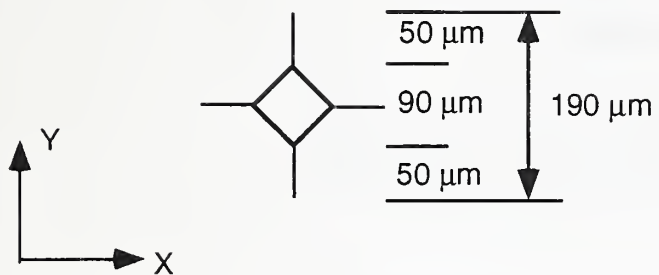


Fig. 11 (b)

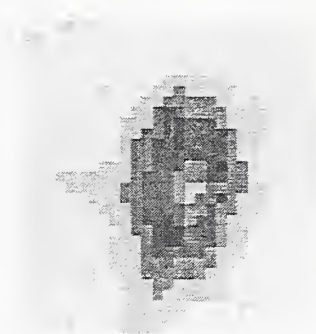


Fig. 11 (a)

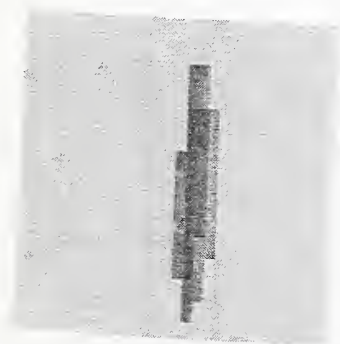


Fig. 11 (c)

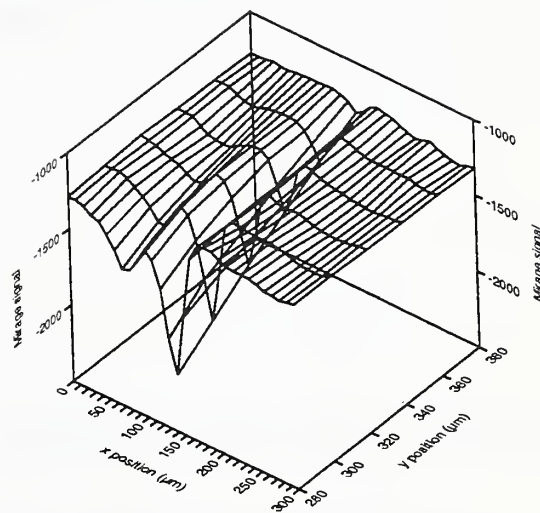


Fig. 12

Appendix 2

“Effect of Grain Size on Grinding Damage in Alumina”

Submitted for Publication to

Journal of the American Ceramic Society

January 1995

EFFECT OF GRAIN SIZE ON GRINDING DAMAGE IN ALUMINA

Hockin H. K. Xu^{1,2}, Lanhua Wei³, and Said Jahanmir

National Institute of Standards and Technology

Gaithersburg, MD 20899

For: *Journal of the American Ceramic Society*

January 1995

¹ Member, American Ceramic Society

² Guest Scientist, from School of Mechanical Engineering, Georgia Institute of Technology, Atlanta, GA 30332-0405

³ Guest Scientist, from Department of Physics and Astronomy, Wayne State University, Detroit, MI 48201

ABSTRACT

The effect of grain size on grinding response and grinding-induced subsurface damage is investigated in a series of alumina ceramics with the average grain size ranging from 3 to 35 μm . The grinding forces, surface roughness and grinding-induced subsurface damage are characterized as a function of grain size. The mechanisms of material removal and the types of grinding-induced subsurface damage are directly observed using a bonded-interface sectioning technique. The subsurface damage takes the form of intragrain twin/slip bands and intergranular microcracks. Propagation of these microcracks results in grain dislodgement as the primary mechanism of material removal in grinding. It is found that both the size and the density of grinding-induced subsurface microcracks increase with the grain size. In addition to using optical microscopy on the sections of the ground specimens, a non-destructive thermal wave measurement technique is used directly on the ground surfaces for the detection of grinding-induced subsurface microcracks. The grain size dependence of the microcrack density estimated from the thermal images is found to agree with the results obtained by the bonded-interface technique.

KEY WORDS

abrasive machining, alumina, grain size, grinding, machining damage, subsurface damage, thermal wave measurement

1. INTRODUCTION

Recent studies in our laboratory [1-3] have demonstrated that the ceramic microstructure (e.g. grain size and distribution of second phases) plays a significant role in abrasive machining of ceramics. These grinding studies and other single-point scratching studies [4-7] on a number of materials have shown that the material removal process predominantly involves grain-dislodgement resulting from intergranular microfracture [3-7], rather than chipping due to the extension of subsurface lateral cracks [8-10]. Therefore, the grinding response of these materials is expected to depend on the grain size. In the present study, the influence of grain size on grinding forces, surface roughness, and grinding-induced subsurface damage is examined for alumina.

The influence of grain size on abrasive machining of ceramics is related to the effect of grain size on mechanical properties [11-17]. For example, it has been shown that increasing the grain size of alumina modifies the toughness curve (i.e., toughness as a function of crack size), resulting in an enhanced toughness in the long-crack region (at crack size \gg grain size), but a diminished toughness in the short-crack region (at crack size \sim grain size) [15,16]. In scratching, it has been found that rate of material removal of alumina can be correlated with the toughness in the short-crack region [4,5].

The machinability of alumina is also observed to depend on the grain size [18-23], with coarser grain aluminas showing smaller grinding forces than finer grain aluminas, and the removal rate increasing with the grain size [18,20,21]. However, while previous studies [18,20-22] have provided important information on the effect of microstructure on machining, the alumina materials used in these studies differed not only in grain size, but also in chemical composition, porosity, and grain size distribution. Therefore, the unequivocal effect of grain size on the grinding response has not been established. In the present study, we use alumina ceramics having different grain sizes but the same chemical compositions, nearly full density, and a narrow grain size distribution.

It has been well-documented that grinding often generates subsurface damage with deleterious effects on strength and performance of ceramic components [24-28]. Studies on

strength are usually followed by fractography where the fracture surface is examined to identify the fracture initiation site and to measure the size of the initial machining-induced microcracks responsible for failure [24,25,28]. However, while fractography is a useful technique in revealing fracture origins, stable crack propagation prior to catastrophic failure may add uncertainty to the crack size measurements. In addition, fractography is not a suitable technique for quantifying the density of grinding-induced cracks distributed throughout the near-surface region.

In the present study, two methods are used to characterize the grinding-induced subsurface damage. First, we use a bonded-interface technique [3,17] to directly observe the subsurface damage generated by grinding in a series of aluminas with different grain sizes. Second, we use a thermal wave measurement technique [29-32], a non-destructive evaluation method, to detect the grinding-induced subsurface microcracks. This technique uses an intensity-modulated laser beam to locally heat the surface and a secondary laser beam to probe the temperature gradient of the air above the heated region. This technique is, in principle, sufficiently sensitive for the detection of surface and near-surface microcracks, because the microcracks can change the local heat flux. This thermal wave measurement technique has been recently used to detect and quantify microcracks in indentation of ceramic materials [31,32]. The density of subsurface microcracks deduced from the thermal wave measurements is then compared with a similar quantity obtained using the bonded-interface technique. These results, in addition to the measurements of grinding forces and roughness values of ground surfaces, are evaluated as a function of grain size.

II. EXPERIMENTAL PROCEDURE

1. Materials

The polycrystalline alumina samples used in the present study were obtained from an earlier study on the effect of grain size on toughness [15]. A high purity alumina powder was doped with a small amount of MgO (atomic ratio of Mg/Al = 500×10^{-6}) and was prepared for sintering in class A-100 clean room conditions. The compacts were pressureless-sintered at 1550 °C for 30

minutes to produce specimens with a density greater than 99% of the theoretical density. The specimens were then heat-treated at prescribed hold times and temperatures to obtain various grain sizes with uniform and equiaxed grain structure and a narrow grain size distribution [15]. The average grain sizes of the specimens selected for use in the present study ranged from 3 to 35 μm (with average grain sizes of 3, 9, 15, 21, and 35 μm) as determined by a linear intercept method[33].

The toughness curves of these aluminas were characterized earlier by Chantikul et al. [15]. The toughness values were calculated, using a grain-bridging model, from strength measurements performed in biaxial fracture tests on samples indented at various loads to produce a wide range of indentation crack sizes. Their results showed that, in these aluminas, the long-crack toughness increases with the average grain size; but the short-crack toughness decreases as the grain size is increased.

The hardness of these aluminas was determined by scratching with a conical diamond indenter under two loads of 10 and 40 N [6]. The scratch hardness was then calculated by dividing the normal load by the square of the scratch width [6]. The effect of grain size on hardness of the selected aluminas are shown in Fig. 1. As shown in the figure, the hardness decreases as the grain size is increased from 3 to 9 μm ; but a further increase in the grain size from 9 to 35 μm has no effect on the hardness.

2. Grinding Experiments

The alumina specimens were machined into test bars with dimensions of 2.5 x 2.5 x 20 mm for the grinding experiments. Grinding was performed on the test bars with a surface grinder using a resin bonded 320 grit peripheral diamond wheel. The wheel was dressed with a porous alumina dressing stick before grinding. A soluble-oil grinding fluid (Cimperial HD90, Cincinnati Milacron, Cincinnati, OH)* was used. Grinding was performed at a wheel surface speed of 37 ms^{-1} and a

* Information on product names, manufacturers and suppliers is included in this paper for clarity. This does not imply endorsement by the National Institute of Standards and Technology.

constant table speed of 0.12 ms^{-1} . The test bars were ground along the specimen length on the $2.5 \times 20 \text{ mm}$ side; and the full specimen width (2.5 mm) was ground without using cross-feed. The depth of cut was varied from 2.5 to $40 \text{ }\mu\text{m/pass}$. At each depth of cut, six passes were made to establish a steady-state condition before force measurements were made. Normal and tangential grinding forces were measured with a Kistler piezoelectric dynamometer and recorded by a personal computer. The surface roughness of the ground surfaces was measured with a stylus surface profilometer.

3. Observation of Subsurface Damage

A bonded-interface technique as described elsewhere [3,17] was used to directly observe the subsurface grinding damage. The polished surfaces ($2.5 \times 20 \text{ mm}$) of a pair of test bars from each grain size were bonded together with a thin layer of adhesive (Loctite Corp., Newington, CT). Clamping pressure was applied during bonding to ensure a narrow interface ($< 1 \text{ }\mu\text{m}$ thick) and to avoid artificial damage at the interface during grinding. Two sets of bounded-interface specimens were prepared for each grain size. In the first set, grinding was performed parallel to the bonded-interface, while in the second set, the grinding direction was perpendicular. In both cases, the depth of cut was equal to $40 \text{ }\mu\text{m/pass}$. The test bars were subsequently separated by melting the adhesive on a hot plate. The specimens were then cleaned with acetone and alcohol. An optical microscope with Nomarski interference illumination and a scanning electron microscope (SEM) were used to examine the surface and subsurface grinding-induced damage.

4. Thermal Wave Measurement

The experimental setup used in the present study, which is based on the optical beam deflection method [29] (also called the “mirage effect” method), has been described elsewhere [31,32]. An argon-ion laser beam was chopped by an acousto-optic modulator at a certain frequency and was focused on the sample surface to provide a localized periodic heat source. A He-

Ne laser probe beam was directed at a near-grazing angle to the surface at the focal spot area of the heating beam and was refracted by the time-varying gradient in the index of refraction of the air. The deflection of the probe beam was monitored through the measurement of both magnitude and phase of the deflection by a position-sensitive quad-cell detector. The output voltage was amplified and fed into two separate vector lock-in amplifiers: one to monitor the deflection normal to the surface; the other to monitor the deflection parallel to the surface, i.e., the transverse deflection. The signals obtained from the lock-in amplifiers were digitized and stored in a personal computer for later analysis.

The radius of the heating beam used in the present study was 5 μm and that of the probe beam was 8 μm . An x-y stage, controlled by a personal computer, was used to scan the specimens in order to obtain thermal wave images of the surfaces under study. A step size of 10 μm was used in both x and y directions. Since the penetration depth of the thermal waves is related to the modulation frequency, changing the frequency changes the detection depth. In the present study, two frequencies of 50 kHz and 500 Hz were used, corresponding to penetration depths of 10 and 100 μm , respectively.

III. RESULTS

1. Grinding Force and Surface Roughness

Grinding force measurements for the aluminas with different grain sizes ranging from 3 to 35 μm are shown in Figs. 2a and 2b, where the normal and tangential grinding forces per unit specimen width are plotted against the depth of cut. Each data point in the plot is the average of four measurements with the error bars showing the standard deviation. It can be seen that both the normal and the tangential grinding forces increase with the depth of cut. To illustrate the grain size effect, the normal and tangential grinding forces (F_n and F_t) for a depth of cut equal to 40 $\mu\text{m/pass}$ are plotted against the grain size in Fig. 3. It is observed that the grinding forces decrease as the grain size is increased from 3 to 9 μm . However, as the grain size is increased further, the grinding

forces remain constant and independent of grain size. Note that this trend is similar to the effect of grain size on hardness in Fig. 1.

The surface roughness after grinding at a depth of cut equal to 40 $\mu\text{m}/\text{pass}$ are shown in Fig. 4. Each data point is the average of six traces obtained at different positions on the ground surfaces, with each trace about 2 mm in length. The direction of the traces was normal to the grinding direction. It can be seen that the arithmetic average roughness, R_a , increases with the grain size. Varying the depth of cut from 2.5 to 40 $\mu\text{m}/\text{pass}$ did not produce a significant effect on the surface roughness values.

2. Subsurface Damage

The grinding-induced subsurface damage observed using the bonded-interface technique is shown in Figs. 5a-e for grain sizes of 3, 9, 15, 21 and 35 μm , respectively. For the sections shown in this figure, grinding was performed perpendicular to the bonded interface using a depth of cut equal to 40 $\mu\text{m}/\text{pass}$. Grinding parallel to the bonded interface produced a similar type of damage. The subsurface damage in the fine grain alumina (grain size = 3 μm) in Fig. 5a is not easily observable. However, subsurface damage in the form of intragrain twin/slip bands and intergranular microcracks is observed in Fig. 5e for the coarse grain alumina (grain size = 35 μm). This is more clearly seen at a higher magnification in Fig. 6a, which shows a grain boundary microcrack, and in Fig. 6b, which shows a microcrack together with intragrain twin/slip bands.

In Figs. 5a-e, the extent of subsurface damage (i.e., both the length and the number of subsurface microcracks) appears to increase with the grain size. The length of cracks normal to the surface is an important parameter, due to the effect of such cracks on strength in flexure testing. The maximum depth of microcracks were estimated by first identifying the four deepest cracks normal to the surface in the section views for each grain size. The length of these microcracks were then averaged to give the maximum depth of microcracks. The results plotted in Fig. 7 show that the maximum depth of microcracks is proportional to the average grain size.

The subsurface microcrack density was estimated by calculating the fraction of microcracked grain facets, defined as the number of cracked grain boundary facets, N_c , divided by the total number of grain facets, N_f . To estimate N_c , first the total length of microcracks, L_t , was calculated by measuring and adding together the lengths of all the microcracks observed on the sections for each grain size. Then, L_t was divided by the average facet size to give N_c . The average facet size was taken as one grain radius, and the total number of facets were obtained by assuming the grain structure to be a two-dimensional hexagonal array. For this arrangement, the total number of facets equals to three times the total number of grains within a two-dimensional region one grain below the surface. The estimated fraction of microcracked grain facets is plotted in Fig. 8 as a function of the inverse square root of the grain size. As the figure shows, the fraction of microcracked facets (i.e., the microcrack density) increases as the grain size is increased. It is acknowledged that what is important here is the *relationship* between the microcrack density and the grain size. The actual magnitude of the microcrack density depends on the simplifying assumptions made in the estimation.

3. Characterization of Grinding Damage by Thermal Wave Measurement

While the simple estimation of microcrack density in the preceding section is based on observations made on the two-dimensional cross-sections of the bonded-interface specimens, the following thermal wave technique estimates the volume density of subsurface microcracks.

Figure 9 shows a series of thermal images taken on the ground surfaces of alumina samples with different grain sizes. The modulation frequency was 500 Hz corresponding to a penetration depth of about 100 μm . These images were prepared with the same contrast to allow a comparison between the signals obtained from the samples. The thermal wave images in Fig. 9 show darker spots corresponding to larger amplitude signals generated as a result of localized high-temperature regions. To eliminate the possibility that the high-temperature regions are associated with intrinsic

microstructural features, thermal wave images of polished specimens were also taken. The results indicated a uniform temperature field upon heating, confirming that the high-temperature regions in Fig. 9 are due to grinding-induced damage.

The high temperature regions in Fig. 9 could be related to either surface features, such as pits associated with grain-pullout, or subsurface features, such as microcracks beneath the ground surface. To evaluate the first possibility, the ground surfaces of selected samples were examined in the SEM after drawing two perpendicular reference lines on the surfaces. The same areas on the ground surfaces were subsequently evaluated by thermal wave.

Figure 10 shows an SEM micrograph and the corresponding thermal wave image of the ground surface of the alumina with a grain size of 35 μm . Grinding grooves and the pits associated with grain-pullout are visible in Fig. 10a. The dark marks produced by ink are seen along the right and bottom edges in Fig. 10a and are indicated by the two perpendicular lines. The same ink marks are also visible on the thermal wave image in Fig. 10b.

Point-to-point comparison between the SEM micrograph in Fig. 10a and the thermal image in Fig. 10b can now be made. The darker spots, designated as “1” and “2” in the thermal wave image correspond to relatively smooth areas on the ground surface, also identified in the SEM micrograph by “1” and “2”. On the other hand, the pits associated with grain-pullout in the SEM micrograph, identified as “3” and “4”, correspond to the background signal in the thermal wave image. These point-to-point comparisons suggest that the high-temperature regions in the thermal wave images are not caused by surface-related features and, therefore, may be related to subsurface grinding-induced damage.

In order to confirm that the darker spots in the thermal wave images are associated with subsurface damage, different modulation frequencies were used to vary the thermal wave penetration depth. The thermal wave images in Figs. 11a and b were obtained at two different frequencies of 500 Hz and 50 kHz, corresponding to penetration depths of $\approx 100 \mu\text{m}$ and $10 \mu\text{m}$, respectively. Both images were obtained from the same area on the ground surface of the alumina

with grain size of $35\text{ }\mu\text{m}$. Fewer high-temperature regions are observed in the thermal wave image corresponding to a penetration depth of $\approx 10\text{ }\mu\text{m}$, Fig. 11b, indicating that most of the high-temperature regions in Fig. 11a are related to features deeper than $10\text{ }\mu\text{m}$. This observation supports the suggestion that the high-temperature regions in the thermal images are associated with subsurface features. Since a recent study [32] demonstrated that in thermal wave measurement the heat flow is disturbed by subsurface microcracks but not by intragrain twin/slip bands, the dark spots in the thermal wave images must be associated with subsurface microcracks.

The thermal wave images in Fig. 9 can be used to estimate the density or fractional area of grinding-induced subsurface microcracks. This is accomplished by first estimating the total area of the dark spots (i.e., high-temperature regions) in a thermal wave image having a signal amplitude larger than a chosen threshold, and then dividing this area by the area of the thermal wave image. The threshold was chosen so that the fractional area of the dark spots would be zero for the alumina with the grain size of $3\text{ }\mu\text{m}$ (Fig. 9a), and just begin to increase above zero for the alumina with a grain size of $9\text{ }\mu\text{m}$ (Fig. 9b). The results of the estimated fractional area of subsurface microcracks are plotted in Fig. 12 as a function of the inverse square root of the grain size. It is again acknowledged that the emphasis here is on the *relationship* between the fractional area of microcracks and the grain size. This relationship, shown in Fig. 12, is similar to the relationship between the fraction of microcracked facets and the grain size (Fig. 8) obtained from the section views.

IV. DISCUSSION

We have demonstrated in the present study that grain size has a strong influence on grinding of alumina ceramics. The grinding response (i.e., grinding force, surface roughness, and both size and density of subsurface microcracks) was shown to be strongly influenced by the grain size. In addition, a thermal wave measurement technique was demonstrated to be a feasible technique for the detection of grinding-induced subsurface microcracks.

The relationship between the grinding force and the grain size (Fig. 3) is similar to the grain size dependence of hardness of the same aluminas (Fig. 1). This suggests that the grinding force of alumina is related to the hardness. A similar result was recently shown for a series of silicon nitride ceramics [34].

A recent study [23] on grinding of aluminas showed a monotonic decrease in the grinding force with increasing grain size from 1 to 12 μm , in agreement with the observations in the present study that grinding force decreases with increasing grain size from 1 to 9 μm . In another study [22], the grinding force was found to be the same for two aluminas having the same composition but different grain sizes of 20 and 40 μm . This is also consistent with the present results showing that the grinding force is independent of the grain size for aluminas with average grain sizes ranging from 9 to 35 μm .

A fundamental issue in this investigation is the nature of subsurface machining damage. Related to this issue is the mechanism of material removal. The modes of grinding-induced subsurface damage was identified in the present study as grain boundary microfracture and intragrain twin/slip bands (Figs. 5 and 6). However, previous studies [8,26,27] have suggested lateral and median cracks as the form of machining-induced subsurface damage in analogy to indentation-induced cracks. Based on this suggestion, chipping produced by the extension of lateral cracks has been proposed as the mechanism of material removal in machining of ceramics [8-10]. Similarly, strength degradation in machining has been assumed to be related to the presence of median cracks [26]. While the analogy between indentation and machining may be applicable to brittle materials such as glasses, it does not seem to agree with the experimental observations on the polycrystalline aluminas in the present study, where material removal occurs by grain dislodgement. As a result of material removal by grain dislodgement, we might expect the surface roughness to increase with the grain size. This was in fact observed in the present study (Fig. 4) and also by Roth et al. [23].

In the present study, the depth of microcracks, which would cause a reduction in strength,

was found to increase with the grain size. However, in previous studies [18,24, 25,28] the size of the subsurface machining-induced flaws, based on fractography observations, was determined to be independent of the grain size. This discrepancy is possibly a result of stable crack propagation prior to failure in fracture testing that may have added uncertainty to the fractography measurements. In comparison, the bonded-interface sectioning technique used in the present study provides a simple and reliable means for revealing the nature of subsurface machining damage and the size of subsurface microcracks.

It has been suggested [17] that the intergranular microcracks are generated as a result of stress concentrations due to the intersection of twin/slip bands with the grain boundaries. Formation of microcracks is expected to be easier in coarse grain aluminas than in finer grain aluminas. The fraction of microcracked grain boundary facets (or the density of intergranular microcracks) has been related to the grain size by Fu and Evans [35] based on the combined influence of thermal mismatch residual stresses and applied stress. A similar relationship can be obtained by considering the influence of grain size on the toughness-curves of aluminas, since the toughness corresponding to small cracks (equivalent to the grain size) is smaller for coarse grain aluminas than for finer grain aluminas [15,16]. The Fu and Evans model predicts the microcrack density to be linearly proportional to the inverse square root of the grain size [35]. The experimental results obtained from the observations of the subsurface microcracks on the bonded-interface sections (Fig. 8) and those determined by thermal wave measurements (Fig. 12) are in agreement with the prediction of the model. The intersection of the straight line with the horizontal axis in Figs. 8 and 12 suggests a threshold grain size of about 8 μm for microcracking under the specific grinding condition used in the present study. The trend of the microcrack density with grain size obtained from the bonded-interface section views (Fig. 8) agrees with that deduced from the thermal wave images (Fig. 12). However, differences between the two methods should be recognized. The former examines two-dimensional sections while the later samples three-dimensional regions below the ground surface.

The thermal wave measurement technique presents itself as a powerful technique for non-destructive detection of subsurface cracks and potentially for quantifying the density of grinding-induced subsurface microcracks. Although the quantification procedure used in the present study involves certain simplifying assumptions, the thermal wave results agree with the measurements by the bonded-interface technique and the prediction from the Fu and Evans microcrack model [35]. This supports the applicability of the thermal wave technique as a non-destructive method for detecting and quantifying the subsurface cracks in machining of ceramics. It is acknowledged that further study is required to evaluate three important issues. First, it should be recognized that the thermal wave measurement technique may not be effective in detecting tightly closed cracks since the heat flow is not greatly disturbed by such cracks. The second issue is related to the directionality of the cracks. The thermal wave images in the present study were obtained from the normal component of the deflected probe beam, which is not sensitive to microcracks that are perpendicular to the surface [31]. Therefore, the dark spots in the thermal wave images correspond more to the microcracks inclined or parallel to the surface. If the tangential component of the deflected probe beam was used, microcracks normal to the surface would have been detected [31]. However, since this deflection component is sensitive to the surface roughness, it would have been difficult to distinguish the signals from the microcracks and those from the background “noise” due to surface roughness. The third issue is the effect of modulation frequency. That is, a higher frequency results in a better detection resolution, but a smaller detection depth. Therefore, there is a trade-off between the detection depth and the detection resolution. Nevertheless, this investigation has shown that the thermal wave measurement technique can be used for the detection of grinding-induced subsurface damage.

V. SUMMARY

Grain size was shown to have a strong influence on the grinding response of alumina ceramics. Using dense aluminas with different grain sizes but the same compositions and a narrow

grain size distribution, the net effect of grain size was investigated. The grinding force was found to decrease when the grain size was increased from 3 to 9 μm , but became constant when the grain size was further increased from 9 to 35 μm . This trend was correlated with the grain size dependence of hardness.

The mode of grinding-induced subsurface damage in the aluminas was shown to be intragrain twin/slip bands and grain boundary microcracks, rather than lateral and median cracks. The mechanism of material removal was mainly grain dislodgement resulting from grain boundary microfracture. The size of grinding-induced subsurface microcracks was shown to increase with the grain size, rather than independent of grain size.

The thermal wave technique was demonstrated for the first time to be a promising non-destructive technique for the detection of grinding-induced subsurface microcracks. Point-to-point comparison between SEM micrographs and thermal wave images of ground surfaces demonstrated that the thermal wave technique detects subsurface cracks instead of surface-related features such as pits. The density of grinding-induced microcracks deduced from the thermal wave images was found to increase with the grain size. This trend was in agreement with both the observations on the bonded-interface sections and the prediction of a microcracking model.

ACKNOWLEDGEMENTS

The support of the Ceramic Technology Project of the DOE Office of Transportation Technologies and the NIST Ceramic Machining Consortium are acknowledged. The authors gratefully thank B. R. Lawn for fruitful discussions and for providing the alumina specimens. Thanks are also due to L. K. Ives, L. Job, K. Ritchie, and S. Darby for experimental assistance, and G. White for providing helpful comments on the manuscript.

REFERENCES

1. H. H. K. Xu and Said Jahanmir, "Scratching and Grinding of a Machinable Glass-Ceramic with Weak Interfaces and Rising *T*-Curve," *J. Am. Ceram. Soc.*, accepted for publication.
2. H. H. K. Xu, N. P. Padture, and S. Jahanmir, "Effect of Microstructure on Material Removal-Mechanisms and Damage Tolerance in Abrasive Machining of Silicon Carbide," *J. Am. Ceram. Soc.*, submitted for publication.
3. H. H. K. Xu and S. Jahanmir, "Simple Technique for Observing Subsurface Damage in Machining of Ceramics," *J. Am. Ceram. Soc.* **77** [5] 1388-90 (1994).
4. H. H. K. Xu and S. Jahanmir, "Microfracture and Material Removal in Scratching of Alumina," *J. Mater. Sci.*, accepted for publication.
5. H. H. K. Xu, S. Jahanmir and Y. Wang, "Effect of Grain Size on Scratch Interactions and Material Removal in Alumina," *J. Am. Ceram. Soc.*, accepted for publication.
6. H. H. K. Xu and S. Jahanmir, "Effect of Grain Size on Scratch Damage and Hardness of Alumina," *J. Mater. Sci. Lett.*, accepted for publication.
7. H. H. K. Xu and S. Jahanmir, "Transitions in the Mechanism of Material Removal in Scratching of Alumina," *Wear*, submitted for publication.
8. A. G. Evans and D. B. Marshall, "Wear Mechanisms in Ceramics," pp. 439-452 in *Fundamentals of Friction and Wear of Materials*, edited by D. A. Rigney, ASM Metals Park, OH, 1981.
9. S. Malkin and J. E. Ritter, "Grinding Mechanisms and Strength Degradation for Ceramics," *ASME Journal of Engineering for Industry* **111** 167-74 (1989).
10. J. Mukerji and P. K. Das, "Wear of Some Advanced Ceramics under a Sharp Indenter in Unidirectional Sliding," *J. Am. Ceram. Soc.* **76** [9] 2376-78 (1993).
11. I. B. Cutler, "Strength Properties of Sintered Alumina in Relation to Porosity and Grain Size," *J. Am. Ceram. Soc.*, **40** [1] 20-23 (1957).
12. F. P. Knudsen, "Dependence of Mechanical Strength of Brittle Polycrystalline Specimens

- on Porosity and Grain Size," *J. Am. Ceram. Soc.*, **42** [8] 376-87 (1959).
13. R. E. Tressler, R. A. Langensiepen, and R. C. Bradt, "Surface-Finish Effects on Strength vs Grain Size Relations in Polycrystalline Al_2O_3 ," *J. Am. Ceram. Soc.*, **57** [5] 226-27 (1974).
 14. R. W. Rice, S. W. Freiman, and J. J. Mecholsky, Jr., "The Dependence of Strength-Controlling Fracture Energy on the Flaw-Size to Grain-Size Ratio," *J. Am. Ceram. Soc.*, **63** [3-4] 129-36 (1980).
 15. P. Chantikul, S. J. Bannison, and B. R. Lawn, "Role of Grain Size in the Strength and R-Curve Properties of Alumina," *J. Am. Ceram. Soc.* **73** [8] 2419-27 (1990).
 16. B. R. Lawn, *Fracture of Brittle Solids--Second Edition*, Cambridge University Press, Cambridge, U.K., 1993.
 17. F. Guiberteau, N. P. Padture, and B. R. Lawn, "Effect of Grain Size on Hertzian Contact Damage in Alumina," *J. Am. Ceram. Soc.*, **77** [7] 1825-31 (1994).
 18. R. W. Rice and B. K. Speronello, "Effect of Microstructure on Rate of Machining of Ceramics," *J. Am. Ceram. Soc.*, **59** [7] 330-33 (1976).
 19. L. F. Goyette, T. J. Kim, and P. J. Gielisse, "Effect of Grain Size on Grinding High Density Aluminum Oxide," *Ceram. Bull.*, **56** [11] 1018-25 (1977).
 20. R. W. Rice, "Micromechanics of Microstructural Aspects of Ceramic Wear," *Ceram. Engrg. Sci. Proc.*, **6** [7-8] 940-958 (1985).
 21. C. Cm. Wu, R. W. Rice, D. Johnson, and B. A. Platt, "Grain Size Dependence of Wear in Ceramics," *Ceram. Engrg. Sci. Proc.*, **6** [7-8] 995-1011 (1985).
 22. D. B. Marshall, B. R. Lawn, and R. B. Cook, "Microstructural Effects on Grinding of Alumina and Glass-Ceramics," *J. Am. Ceram. Soc.*, **70** [6] C-139-40 (1987).
 23. P. Roth and H. K. Tonshoff, "Influence of Microstructure on Grindability of Alumina Ceramics", pp. 247-261 in *Machining of Advanced Materials*, edited by S. Jahanmir, U.S. Government Printing Office, Washington DC, NIST SP 847, 1993.

24. R. W. Rice, "Machining Flaws and the Strength Grain Size Behavior of Ceramics," pp. 429-54 in *The Science of Ceramic Machining and Surface Finishing II*, edited by B. J. Hockey and R. W. Rice, U.S. Government Printing Office, Washington DC, NBS SP 562, 1979.
25. R. W. Rice and J. J. Mecholsky, Jr., "The Nature of Strength Controlling Machining Flaws in Ceramics," pp. 351-378 in *The Science of Ceramic Machining and Surface Finishing II*, edited by B. J. Hockey and R. W. Rice, U.S. Government Printing Office, Washington DC, NBS SP 562, 1979.
26. D. B. Marshall, A. G. Evans, B. T. K. Yakub, J. W. Tien, and G. S. Kino, "The Nature of Machining Damage in Brittle Materials," *Proc. R. Soc. Lond. A* **385** 461-75 (1983).
27. H. P. Kirchner, "Damage Penetration at Elongated Machining Grooves in Hot-Pressed Si_3N_4 ," *J. Am. Ceram. Soc.*, **67** [2] 127-32 (1984).
28. R. W. Rice, "Effect of Ceramic Microstructural Character on Machining Direction-Strength Anisotropy," pp. 185-204 in *Machining of Advanced Materials*, edited by S. Jahanmir, U.S. Government Printing Office, Washington DC, NIST SP 847, 1993.
29. A. C. Boccara, D. Fournier, and J. Badoz, "Thermo-Optical Spectroscopy: Detection by the 'Mirage' Effect," *Appl. Phys. Lett.*, **36** 130-32 (1980).
30. T. R. Anthony, W. F. Banholzer, J. F. Fleischer, L. Wei, P. K. Kuo, R. L. Thomas, and R. W. Pryor, "Thermal Diffusivity of Isotopically Enriched ^{12}C Diamond," *Phys. Rev. B* **42** 1104-1111 (1990).
31. H. S. Ahn, L. Wei, and S. Jahanmir, "Non-Destructive Detection of Damage Produced by a Sharp Indenter in Ceramics," *Symposium on Measurement and Inspection of Products and Processes*, ASME Winter Annual Meeting, Chicago, IL, 1994, submitted for publication.
32. H. H. K. Xu, L. Wei, N. P. Padture, and B. R. Lawn, "Effect of Microstructural Coarsening on Hertzian Contact Damage in Silicon Nitride," *J. Mater. Sci.*, accepted for

publication.

33. J. C. Wurst and J. A. Nelson, "Linear Intercept Technique for Measuring Grain Size in Two-Phase Polycrystalline Ceramics," *J. Am. Ceram. Soc.*, **55** [2] 109 (1972).
34. S. Jahanmir, T. Hwang, E. P. Whiteman, L. S. Job, and C. J. Evans, "Measurement and Analysis of Forces in Grinding of Silicon Nitride," *Proc. of Tribology Symposium*, ASME, New York, 1995.
35. Y. Fu and A. G. Evans, "Some Effects of Microcracks on the Mechanical Properties of Brittle Solids--I. Stress, Strain Relation," *Acta. Metall.* **33** [8] 1515-23 (1985).

FIGURE CAPTIONS

1. Scratch hardness versus grain size for alumina. Scratches were made at normal loads of 10 and 40 N. Each data point is the average of four measurements and the error bars indicate standard deviations of the measurements (adapted from Ref. 6).
2. (a) Normal and (b) tangential grinding forces as a function of the depth of cut for aluminas with average grain sizes ranging from 3 to 35 μm . Each data point is the average of four measurements and the error bars show the standard deviations of the measurements.
3. Normal and Tangential grinding forces (F_n and F_t) as a function of grain size at a depth of cut equal to 40 $\mu\text{m}/\text{pass}$. Each data point is the average of four measurements and the error bars show the standard deviations of the measurements.
4. Average surface roughness of alumina as a function of grain size at a depth of cut of 40 $\mu\text{m}/\text{pass}$. Each data point is the average of six traces at different positions on the ground surface, with each trace about 2 mm in length. The error bars are the standard deviations of the measurements.
5. Optical micrographs with Nomarski illumination showing section views of subsurface grinding damage in aluminas with grain sizes of (a) 3, (b) 9, (c) 15, (d) 21, and (e) 35 μm .

The depth of cut was 40 $\mu\text{m}/\text{pass}$.

6. Higher magnification section views of subsurface grinding damage in alumina with a grain size of 35 μm at a depth of cut of 40 $\mu\text{m}/\text{pass}$ showing (a) grain boundary microcracks, and (b) a microcrack associated with intragrain shear faults.
7. Grinding-induced subsurface crack depth measured from section views as a function of grain size. Each data is the average of the four deepest cracks within a section region of 10 mm in length, and the error bars are the standard deviations of the measurements.
8. Fraction of microcracked grain boundary facets estimated from the section views as a function of the square root of the grain size. Each data point is the average of five measurements and the error bars are the standard deviations of the measurements.
9. Thermal wave images of ground specimens with grain sizes (a) 3, (b) 9, (c) 15, (d) 21, and (e) 35 μm . The size of each image is 450 x 380 μm . Grinding direction was horizontal and the depth of cut was equal to 40 $\mu\text{m}/\text{pass}$.
10. (a) SEM micrograph and (b) thermal wave image of the ground surface of alumina with grain size 35 μm . Magnification of (b) is same as (a). The axes at the lower right corner indicate the ink marks. Arrows “1” and “2” point at relatively smooth areas on the ground surface in (a) and the corresponding dark spots in (b). Arrows “3” and “4” point at pits produced by grain pullout on the ground surface in (a) and the corresponding normal background areas in (b). Grinding direction was horizontal and the depth of cut was equal to 40 $\mu\text{m}/\text{pass}$.
11. Thermal wave images of the ground surface of alumina with grain size 35 μm at a modulation frequency of (a) 500 Hz, and (b) 50 kHz. The size of each image is 500 x 250 μm . Grinding direction was horizontal and the depth of cut was equal to 40 $\mu\text{m}/\text{pass}$.
12. Thermal wave measurement of microcrack density as a function of the square root of the grain size. Each data point is the average of four measurements and the error bars are the standard deviations of the measurements.

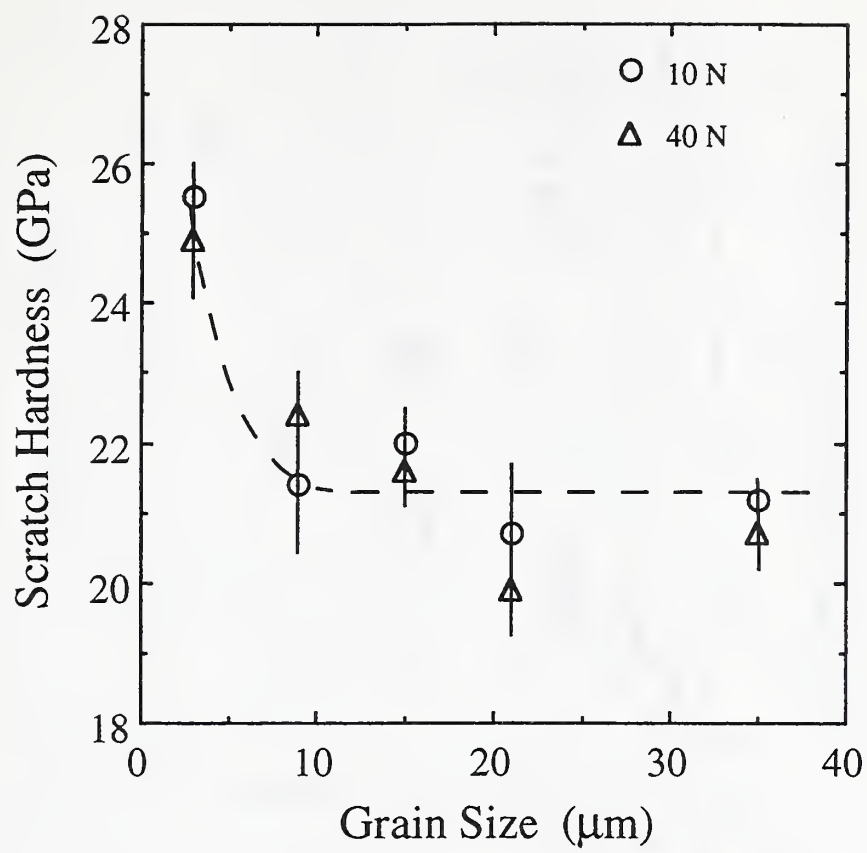


Fig. 1

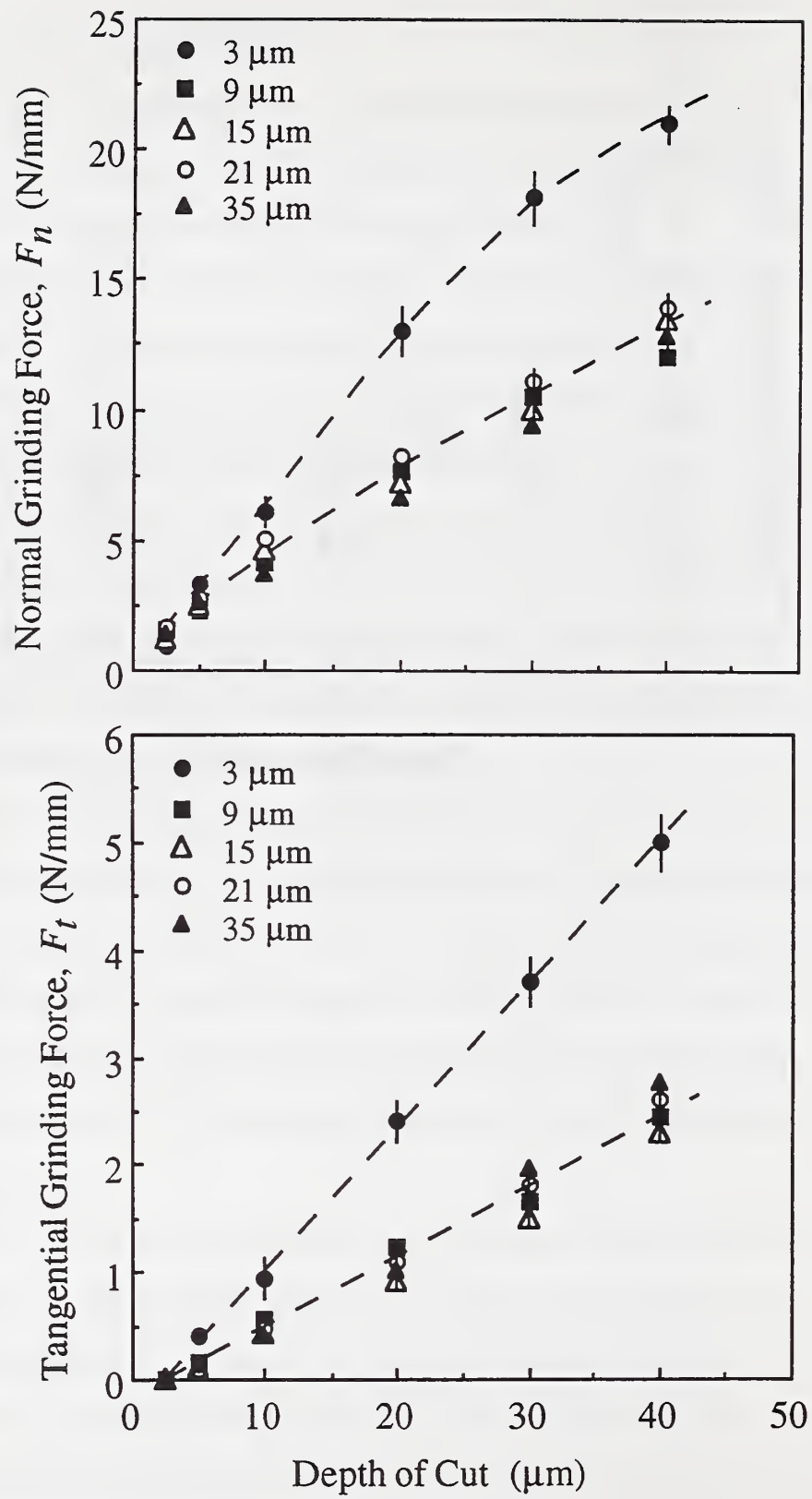


Fig. 2

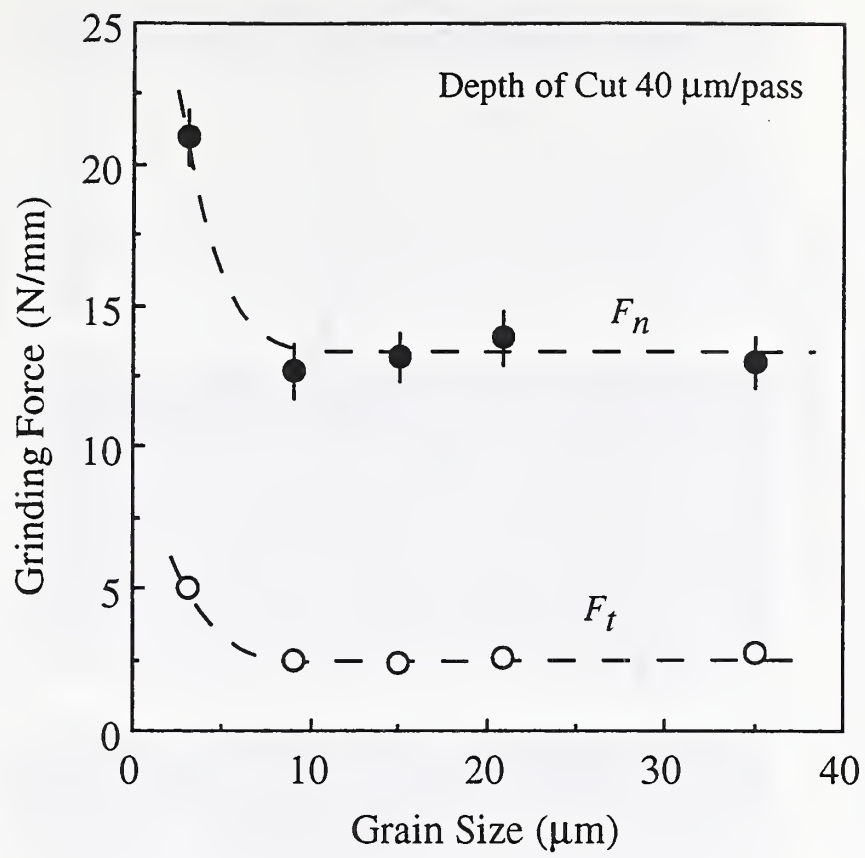


Fig. 3

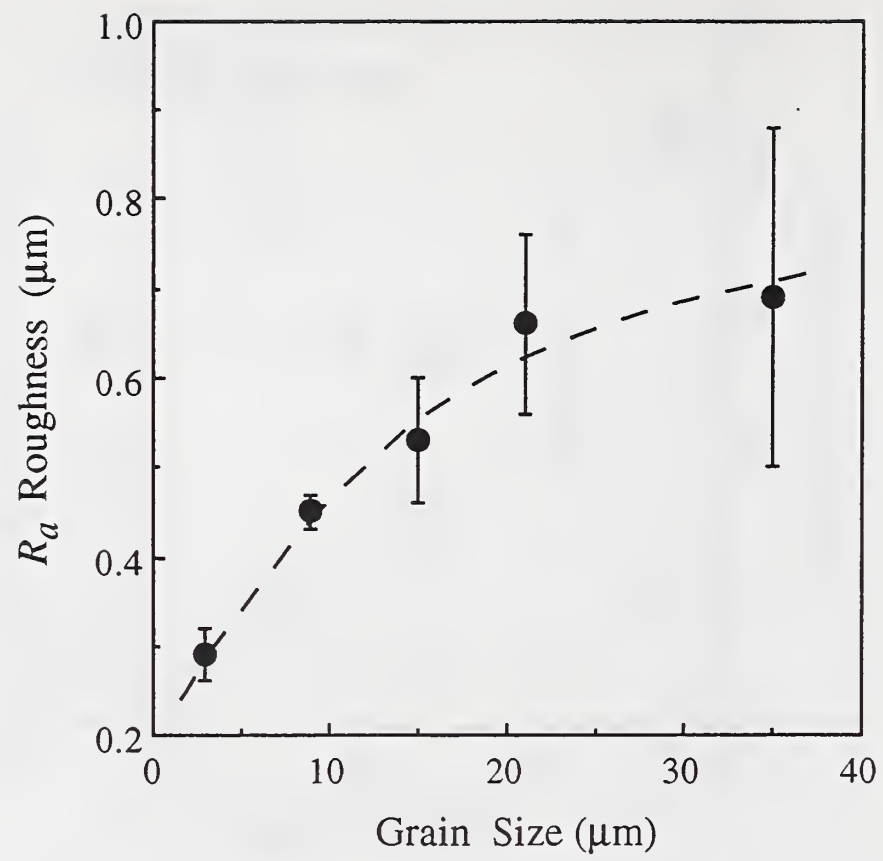
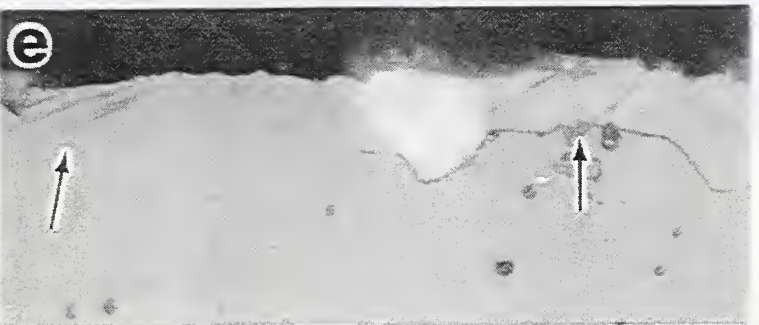
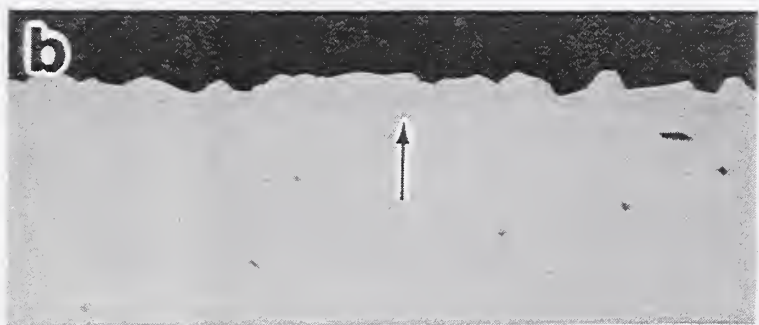
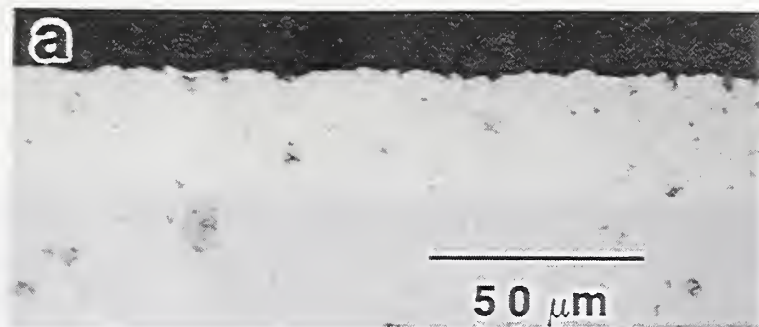
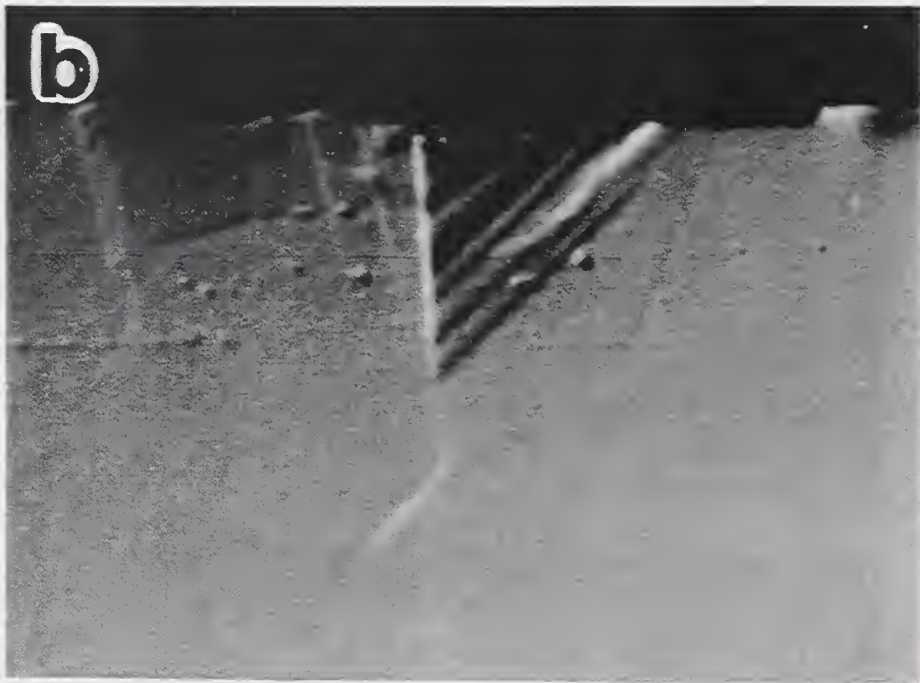
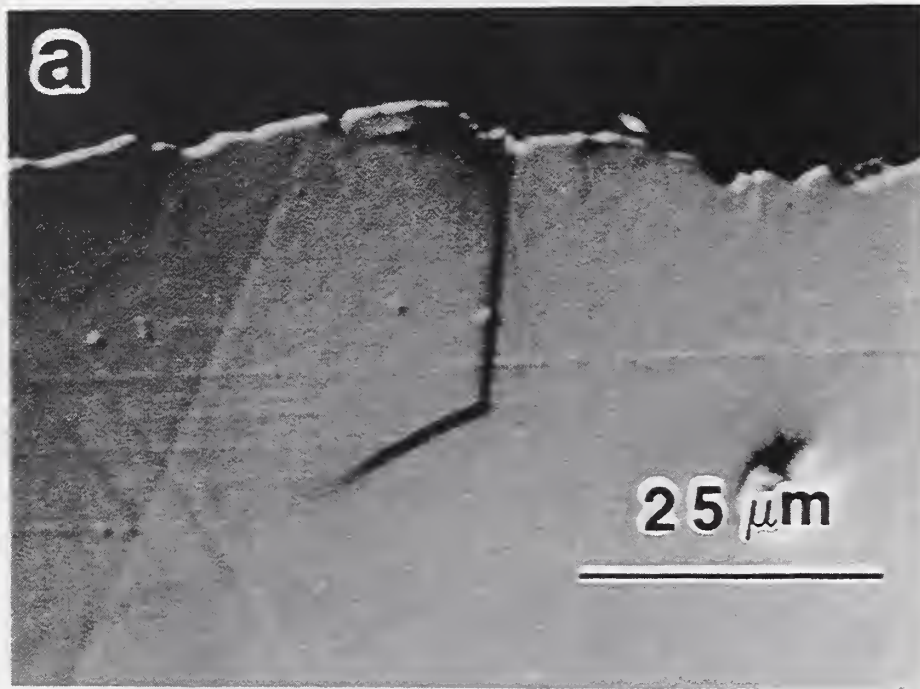


Fig. 4





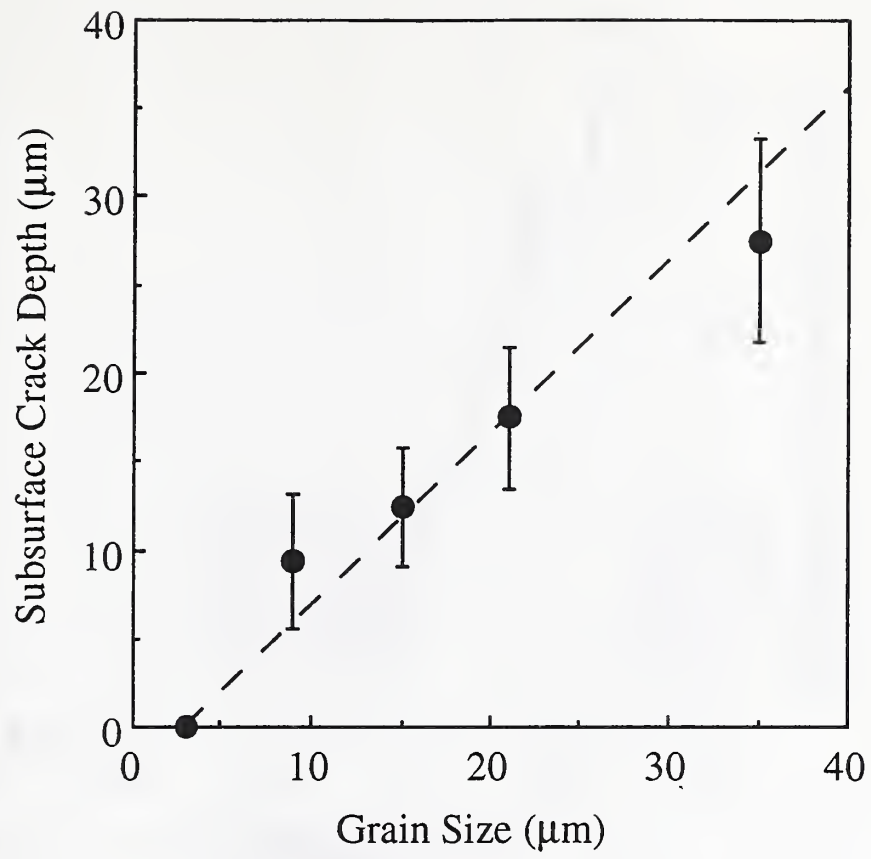


Fig. 7

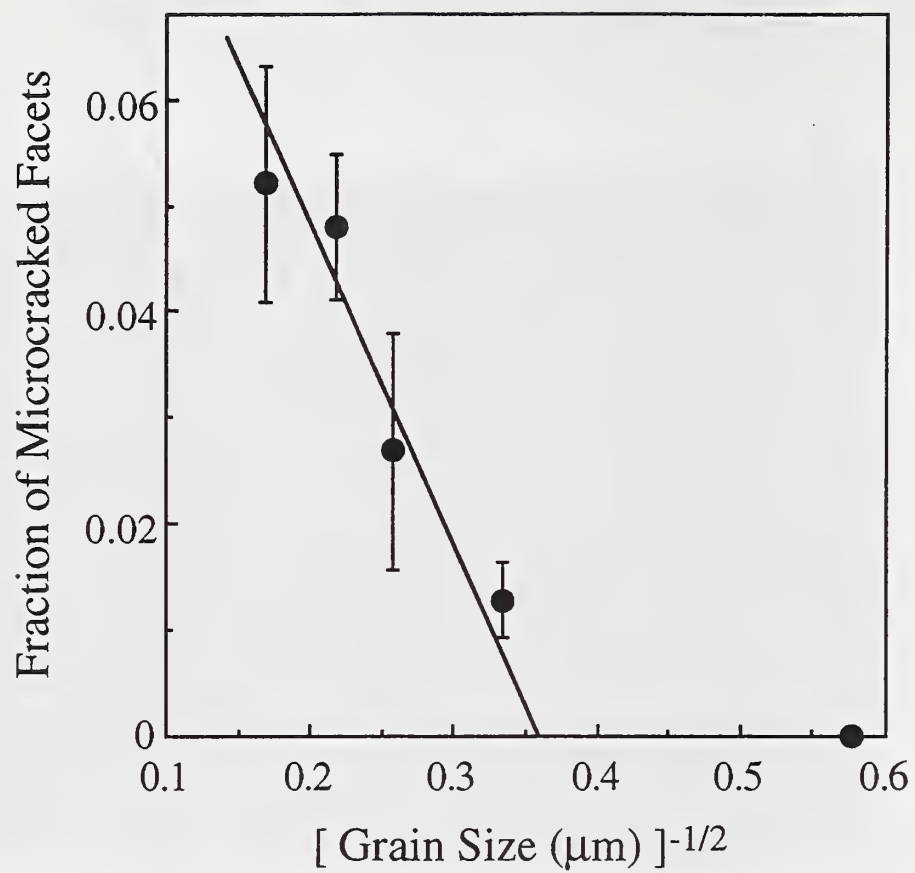


Fig. 8

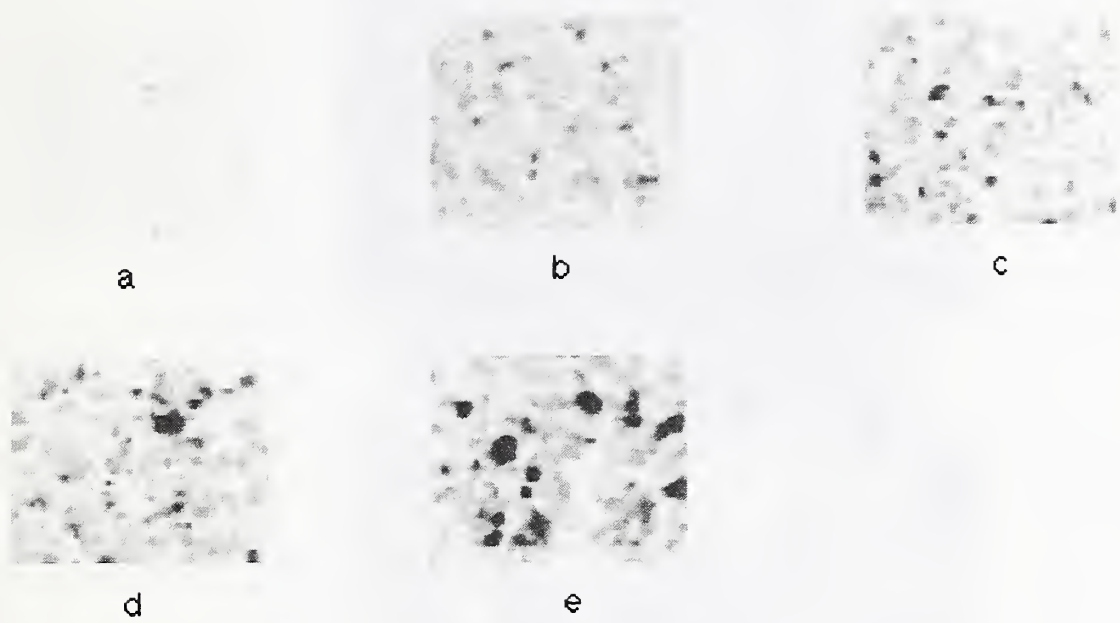


Fig. 9

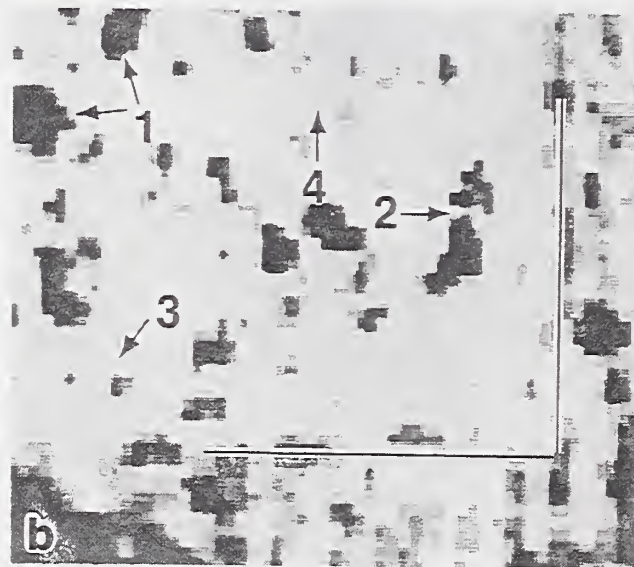
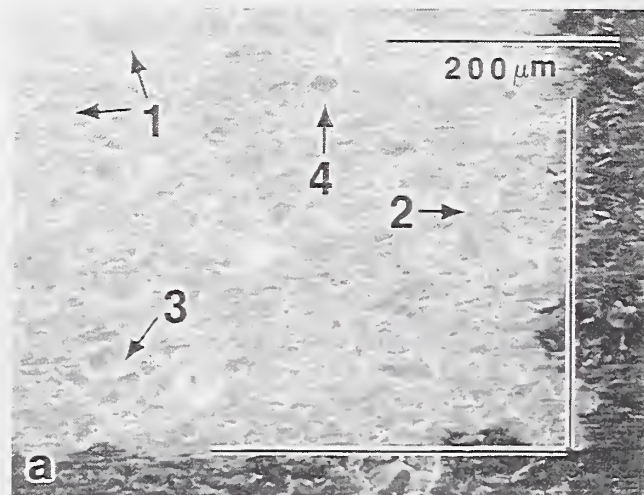
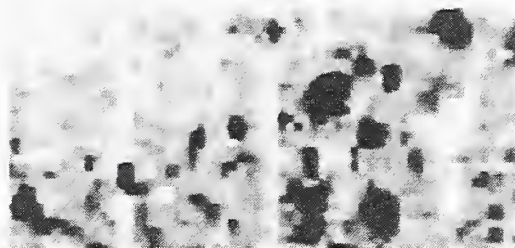


Fig. 10



a



b

Fig. 11

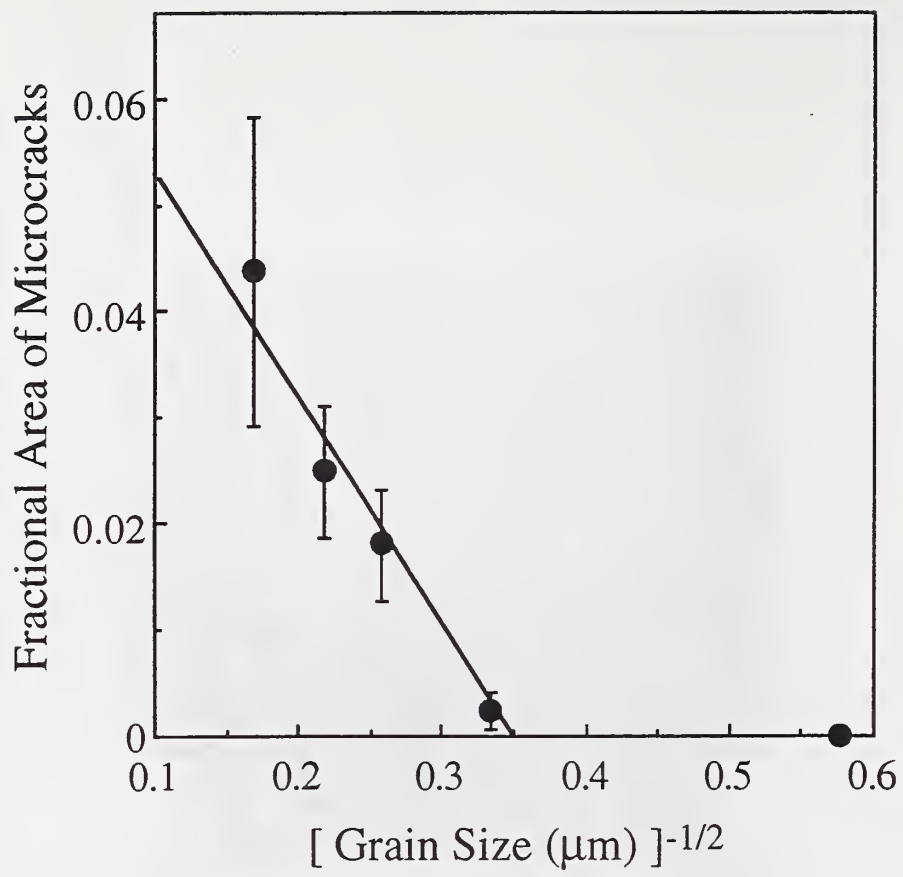


Fig. 12

Appendix 3

“Grinding Force and Microcrack Density in Abrasive Machining of Silicon Nitride ”

Submitted for Publication to

Journal of Materials Research

February 1995

Grinding Force and Microcrack Density in Abrasive Machining of Silicon Nitride

Hockin H. K. Xu ¹, Lanhua Wei ², Said Jahanmir

Ceramics Division

National Institute of Standards and Technology

Gaithersburg, MD 20899

For: *Journal of Materials Research (Communication)*

March 1995

-
- ¹ Guest Scientist, from School of Mechanical Engineering, Georgia Institute of Technology, Atlanta, GA 30332-0405
- ² Guest Scientist, from Department of Physics and Astronomy, Wayne State University, Detroit, MI 48201

ABSTRACT

The relationship between grinding forces and the material's resistance to microfracture is investigated in abrasive machining of silicon nitride ceramics. Surface grinding is performed on two forms of silicon nitride with different microstructures and the grinding forces are measured. In addition, single-point scratching is performed on polished surfaces to amplify the damage associated with the action of an individual abrasive particle in grinding. A thermal wave measurement technique is then used on the cross-sections to quantify the density of subsurface microcracks associated with scratching. Compared to a fine-grain silicon nitride, the density of microcracks in a coarse-grain silicon nitride is significantly larger, while the grinding force is smaller. The smaller grinding force for the coarse-grain silicon nitride is attributed to the ease of local intergranular microfracture and grain dislodgement during grinding.

Recent studies in our laboratory [1-4] have demonstrated the importance of intergranular microfracture and grain dislodgement in abrasive machining of polycrystalline ceramics. Material removal by lateral crack extension [5] has not been observed to be an active process [1-4]. In surface grinding, the ceramic workpiece is translated toward the grinding wheel at a prescribed table speed and depth of cut. The forces generated between the grinding wheel and the ceramic workpiece during grinding are related to the hardness and toughness of the material [1-4] and, therefore, must be related to the propensity of the material to microfracture and grain dislodgement. The purpose of the present study is to examine the possible correlation between the grinding forces and the material's resistance to intergranular microfracture in abrasive machining of ceramics.

Two forms of silicon nitride were selected for the present study. Both materials were doped with 4 vol% yttria and were hot-isostatically pressed. Elongated grains with an aspect ratio of about 4 were produced by heat treatment. The material with an average grain diameter of 0.5 μm and length of 2 μm was designated as "fine-grain", and that with an average grain diameter of 2 μm and length of 8 μm was designated as "coarse-grain" silicon nitride. The fine-grain silicon nitride had an α to β phase ratio of 30/70, while the coarse-grain material was 100% β phase. Both materials had a porosity of less than 1%. The Vickers hardness values at an indentation load of 10 N were 20.0 and 16.3 GPa, for the fine-grain and the coarse-grain materials, respectively [6]. The standard deviation for the hardness measurements were 1.1 GPa in both cases.

Grinding experiments were performed using a surface grinder and a resin-bonded 80 grit peripheral diamond wheel. The wheel was dressed with an alumina dressing stick before grinding. A soluble-oil grinding fluid was used. The wheel surface speed was 37 m/s and the table speed was 0.12 m/s. The specimens used for grinding had a dimension of 4 x 4 x 20 mm and were ground along the 4 x 20 mm surface. Normal and tangential grinding forces were measured with a piezoelectric dynamometer. The depth of cut was varied from 2.5 to 30 μm /pass. At each depth of cut, six passes were made to establish steady-state conditions before the forces were measured.

The normal and tangential grinding forces (per unit specimen width) as a function of the depth of cut in grinding are plotted in Fig. 1 for the two silicon nitrides. Compared to the fine-grain material, the grinding forces for the coarse-grain silicon nitride are consistently smaller, about 70% of those of the fine grain silicon nitride.

Representative SEM micrographs of the surfaces ground at a depth of cut of 20 μm /pass are shown in Figs. 2A and 2B, for the fine-grain and the coarse-grain silicon nitrides, respectively. The arrows point at sites of microfracture and grain pullout. It can be seen that although the extent of microfracture is more severe in the coarse-grain silicon nitride, the mode of material removal is the same in both materials, i.e., material removal predominantly involves intergranular microfracture and grain dislodgement. In some cases, removal also involves the dislodgement of a number of grains or a portion of an individual grain.

Since the subsurface grinding damage induced by each diamond particle may be too small for detection in these materials, single-point scratching experiments were used under a large load to amplify the extent of the damage associated with grinding. Studies in our laboratory [1-4] have shown that the types of microfracture and damage formation in single-point scratching are similar to those in grinding. A bonded-interface sectioning technique detailed elsewhere [1,7] was used to reveal the subsurface scratching damage. First, specimens with dimensions of 4 x 4 x 20 mm were polished on one rectangular surface with 1 μm diamond paste. The polished surfaces of two specimens of each material were then bonded together by an adhesive. Scratches were made on the top surface across the bonded interface with the sliding direction normal to the interface. Scratches were made with a conical diamond indenter having an apex angle of 120 ° and a spherical tip of about 200 μm , under a constant normal load of 60 N at a sliding speed of about 0.5 mm/s in air with a relative humidity of 40-50%. After scratching, the two specimens were separated and surface and subsurface damage were examined using optical and scanning electron microscopy (SEM).

Scratching damage in the fine-grain and the coarse-grain silicon nitrides produced by a single pass is shown in Figs. 3A and 3B, respectively. The upper micrograph in each case is a view

of the scratched surface and the lower micrograph is the corresponding cross-section. Note that the impression width and the size of the "plastic" zone (designated by p) are larger for the coarse-grain material than for the fine-grain material. This is consistent with the hardness data for the two materials. Examination of the scratches at a higher magnification in the SEM revealed that intergranular microfracture and grain dislodgement occurred in both materials. The lower micrographs in Fig. 3 show median cracks (designated by m) extending from the "plastic" zones. No lateral cracks are observed with the specific load and the indenter geometry used in the present study. Lateral cracks were observed in scratching of a fine-grain alumina [2]. However, the mechanism of material removal in both scratching [2] and grinding [8] was still mainly grain dislodgement, rather than chipping by lateral crack extension [5].

In order to elucidate the mechanism of material removal, the nature of damage in the "plastic" zone was examined in the SEM. Figure 4A shows a few grain-boundary microcracks (indicated by the arrows) together with the median crack (designated by m) in the fine-grain silicon nitride. Figures 4B and 4C show the intergranular microcracks and intragrain twin/slip lines in the coarse-grain silicon nitride.

Quantitative evaluation of the subsurface microcrack density was made by a thermal wave technique, which is based on the optical beam deflection method [9]. This thermal wave technique enables the sampling of a volume of a specimen, rather than only the surfaces. Details of this technique have been described elsewhere [6,8,10]. Briefly, this technique uses an intensity-modulated laser beam to locally heat a specimen under investigation. A second laser beam is used as a probe to monitor the heat diffusion in the specimen through the deflection of the probe beam as a result of the temperature gradient of the air adjacent to the heated surface. This thermal wave measurement technique has been demonstrated to be sufficiently sensitive for the detection [10] and quantification [6,8] of subsurface microcracks because microcracks change the local heat flux. It is capable of detecting not only cracks on the section surfaces, but more importantly cracks beneath the surfaces [8]. In the present study, the subsurface scratching damage on the specimen sections

was examined by the thermal wave technique using a modulation frequency of 10 kHz corresponding to a penetration depth of about 25 μm .

Figures 5A and B show thermal wave images of the sections for the fine-grain and coarse-grain silicon nitrides, respectively. In these images, the background signal level corresponds to a region with uniform thermal property. The signal distinguished from the background is caused by a local alternating temperature rise due to the reflection of thermal waves from heat barriers such as cracks. Note the striking correspondence between these thermal wave images and the optical micrographs of the sections in Fig. 3. The median cracks are also visible in the thermal wave images, but the signal associated with the median crack is not as strong as that associated with the “plastic” zone. In here, the normal deflection component of the probe beam was used since this deflection component is more sensitive to the microcracks distributed within this region. The transverse deflection component, however, is more sensitive to cracks that are normal to the surface being examined, e.g., the median cracks [10].

Since the microcracks disturb the local heat flux, their presence in the plastic zone results in an increase in the magnitude of the thermal wave signal. Therefore, the higher the microcrack density, the larger the magnitude of the signal relative to the undamaged background [6,10]. It is important to note here that the intragrain twin/slip bands were shown to have relatively little effect on the signal magnitude [6]. Therefore, the high-temperature regions associated with the damage zone is primarily due to the presence of microcracks in that region.

In this study the thermal wave penetration depth was about 25 μm ; therefore, the signals are a result of all the microcracks within a volume with a thickness of about 25 μm rather than only the microcracks on the surface of the section. The average microcrack density can be deduced from the thermal diffusivity in the “plastic” zone relative to the undamaged region using the Hasselman equation [11]. The average diffusivity value was simply taken as being inversely proportional to the average signal magnitude within the “plastic” zone. The microcrack density within the “plastic” zone of the coarse-grain silicon nitride was thus estimated to be about 2.2 times more than that of

the fine-grain material.

What is related to the grinding force is not only the microcrack density within the “plastic” zone, but also the size of the zone. Here we define “damage intensity” as being proportional to the microcrack density within the “plastic” zone, times the cross-sectional area of this zone. While the size of the “plastic” zone is related to the hardness, the microcrack density within this zone should depend on the toughness of the material in the short-crack region [12,8]. Therefore, the damage intensity, thus defined, must be related to both hardness and toughness.

The cross-sectional area of the “plastic” zone associated with the coarse-grain silicon nitride is estimated from the thermal wave images to be about 2.3 times more than that of the fine-grain material. The damage intensity in the coarse-grain silicon nitride is then estimated to be about 5 times more than that of the fine-grain material, as shown in Fig. 6. The values of the damage intensity are relative since the absolute values depend on the assumptions of the coefficients in the relationships between signal magnitude, thermal diffusivity and crack density [11]. Nevertheless, the damage intensity is substantially larger in the coarse-grain silicon nitride than that in the fine-grain silicon nitride. This suggests that compared with the coarse-grain silicon nitride, the fine-grain material should have a higher resistance to local microcracking in grinding. This should result in easier removal by grain dislodgement and consequently smaller grinding forces for the coarse-grain silicon nitride. This is, in fact, observed in Fig. 1.

This study, therefore, suggests an intrinsic relation between the grinding force and the material’s resistance to local intergranular microfracture during grinding. Although this conclusion is based only on two silicon nitride materials, an on-going study in our laboratory has shown a consistent correlation between microcracking and grinding force for twenty different ceramic materials. This correlation has important implications concerning microstructural design of ceramics for improved machinability via well-controlled local intergranular microfracture [3,4].

ACKNOWLEDGEMENT

We gratefully thank R. L. Yeckley (Norton Co.) for providing the silicon nitride materials. This research was supported in part by the U. S. Department of Energy-Ceramic Technology Project.

REFERENCES

1. H. H. K. Xu and S. Jahanmir, *J. Am. Ceram. Soc.* **77** [5] 1388 (1994).
2. H. H. K. Xu and S. Jahanmir, *J. Mater. Sci.*, in press.
3. H. H. K. Xu, N. P. Padture, and S. Jahanmir, *J. Am. Ceram. Soc.*, submitted.
4. H. H. K. Xu and S. Jahanmir, *J. Am. Ceram. Soc.* **78** [2] 497 (1995).
5. A. G. Evans and D. B. Marshall, *Fundamentals of Frictions and Wear of Materials* (ASM, Metals Park, OH, 1981), p. 439.
6. H. H. K. Xu, L. Wei, N. P. Padture, B. R. Lawn, and R. Yeckley, *J. Mater. Sci.*, in press.
7. F. Guiberteau, N. P. Padture, and B. R. Lawn, *J. Am. Ceram. Soc.*, **77** [7] 1825 (1994).
8. H. H. K. Xu, L. Wei, and S. Jahanmir, *J. Am. Ceram. Soc.*, submitted.
9. A. C. Boccara, D. Fournier, and J. Badoz, *Appl. Phys. Lett.*, **36** 130 (1980).
10. H. S. Ahn, L. Wei, and S. Jahanmir, *Manufacturing Science and Engineering* (PED-Vol. 68, ASME Press, New York, NY, 1994), p. 923.
11. D. P. H. Hasselman, *J. Composite Mater.*, **12** 403 (1978).
12. B. R. Lawn, *Fracture of Brittle Solids*, (2nd edition, Cambridge University Press, Cambridge, U. K., 1993).

FIGURE CAPTIONS

1. Normal and tangential grinding forces per unit specimen width as a function of the depth of cut, showing lower grinding forces for the coarse-grain silicon nitride compared to the fine-grain silicon nitride. Each data point is the average of four measurements. Error bars show standard deviations of the four measurements.
2. SEM micrographs of the ground surfaces of (A) fine-grain and (B) coarse-grain silicon nitride at a depth of cut of 20 $\mu\text{m}/\text{pass}$. Grinding direction was horizontal. Arrows point at sites of microfracture and grain dislodgement.
3. Scratch damage in (A) fine-grain and (B) coarse-grain silicon nitride produced by a single pass at a load of 60 N. Optical micrographs with Nomarski illumination. Upper halves are surface views and lower halves are section views. Arrow indicates direction of scratching. The subsurface plastic zone is designated by p, and the median crack by m.
4. SEM views of the damage zone for (A) fine-grain silicon nitride, and (B) and (C) coarse-grain silicon nitride. Arrows point at grain-boundary microcracks. The median crack in (A) is designated by m. Intragrain slip bands are visible in (C).
5. Thermal wave images of the subsurface damage zone in (A) fine-grain and (B) coarse-grain silicon nitride. For the fine-grain silicon nitride in (A), the signal magnitude was small. So the images were so adjusted to best show the features for the fine-grain material. The size of each image is 160 x 170 μm .
6. Damage intensity for the fine-grain and coarse-grain silicon nitrides. Error bars show the standard deviations of the three measurements made on each material.

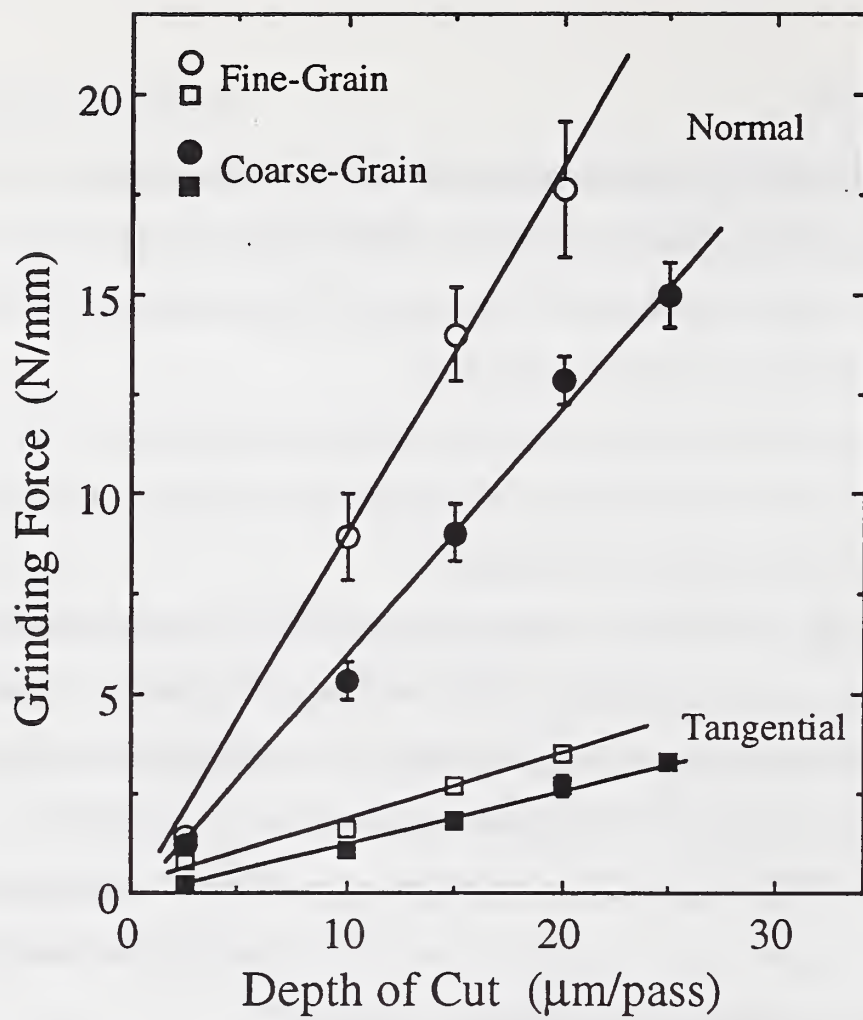


Fig. 1

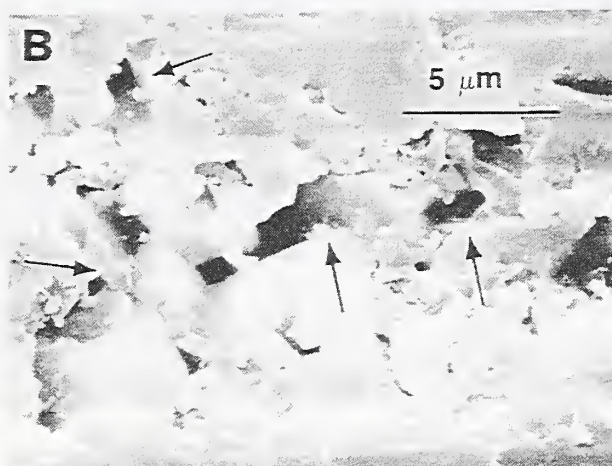
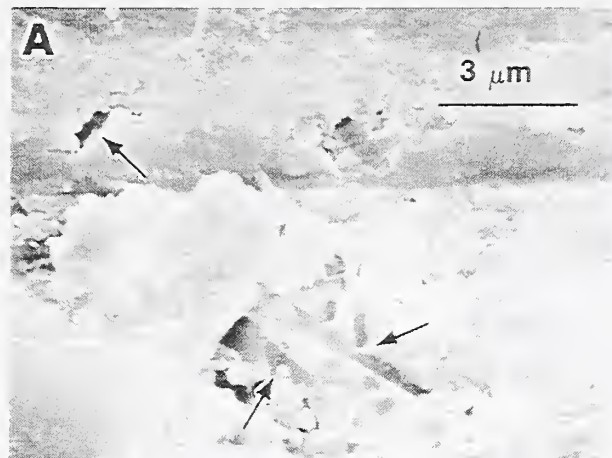


Fig. 2

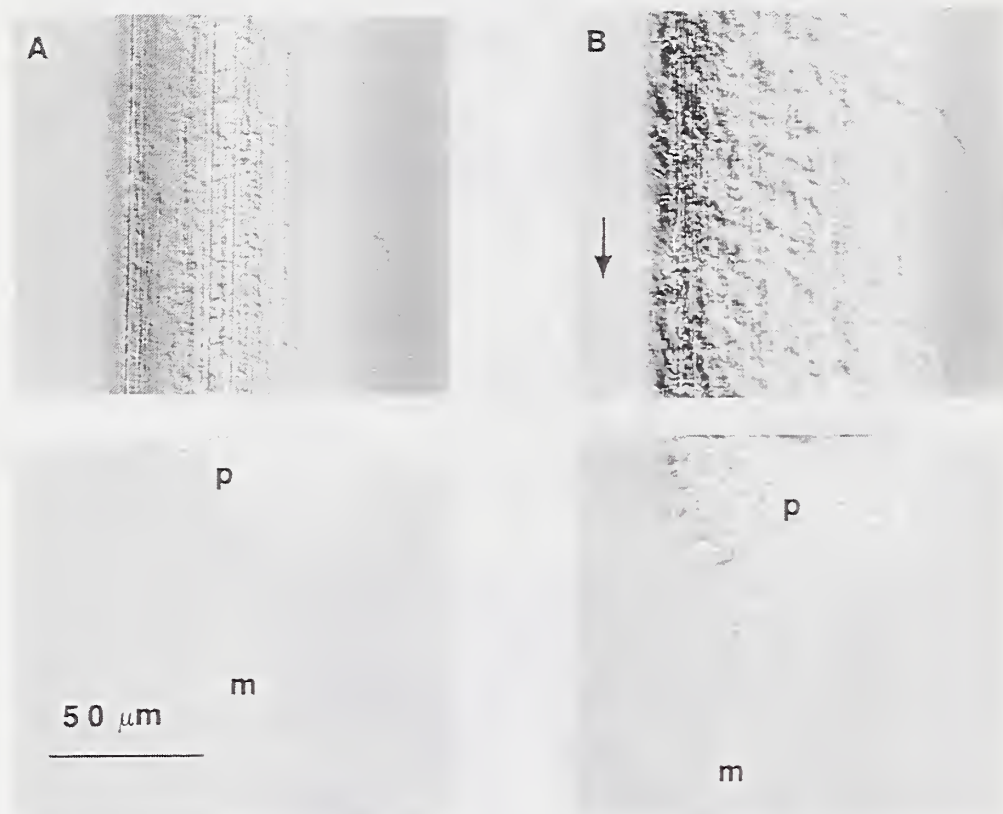


Fig. 3

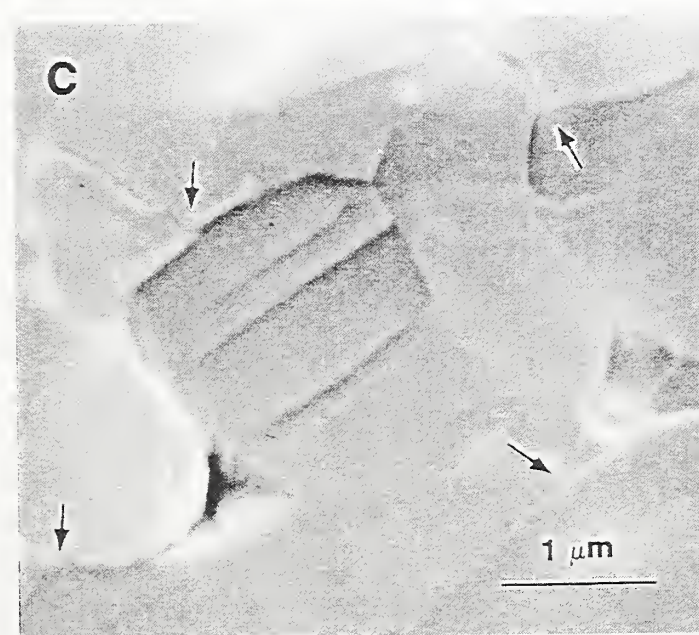
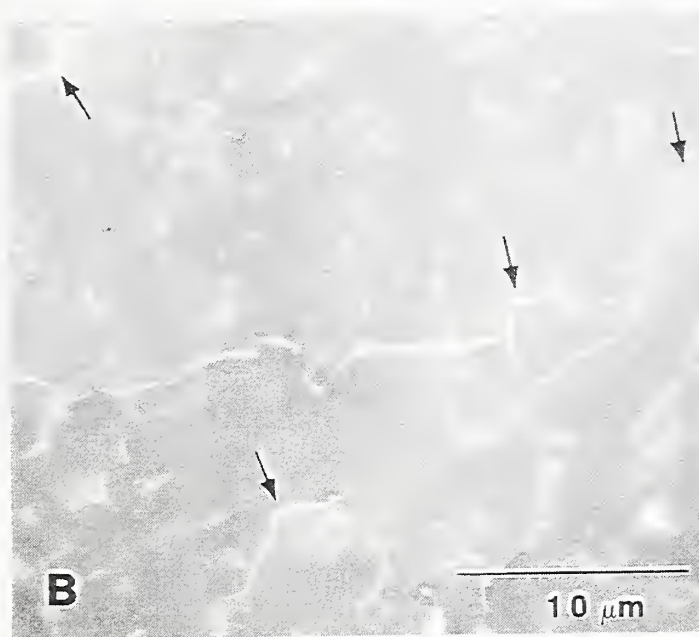
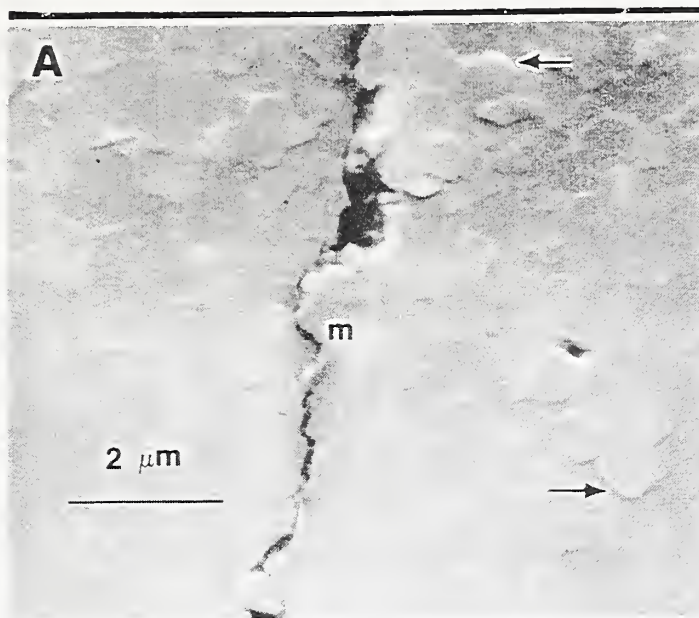


Fig. 4

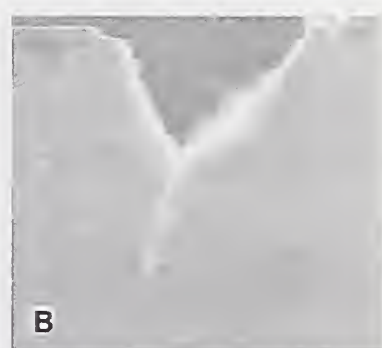


Fig. 5

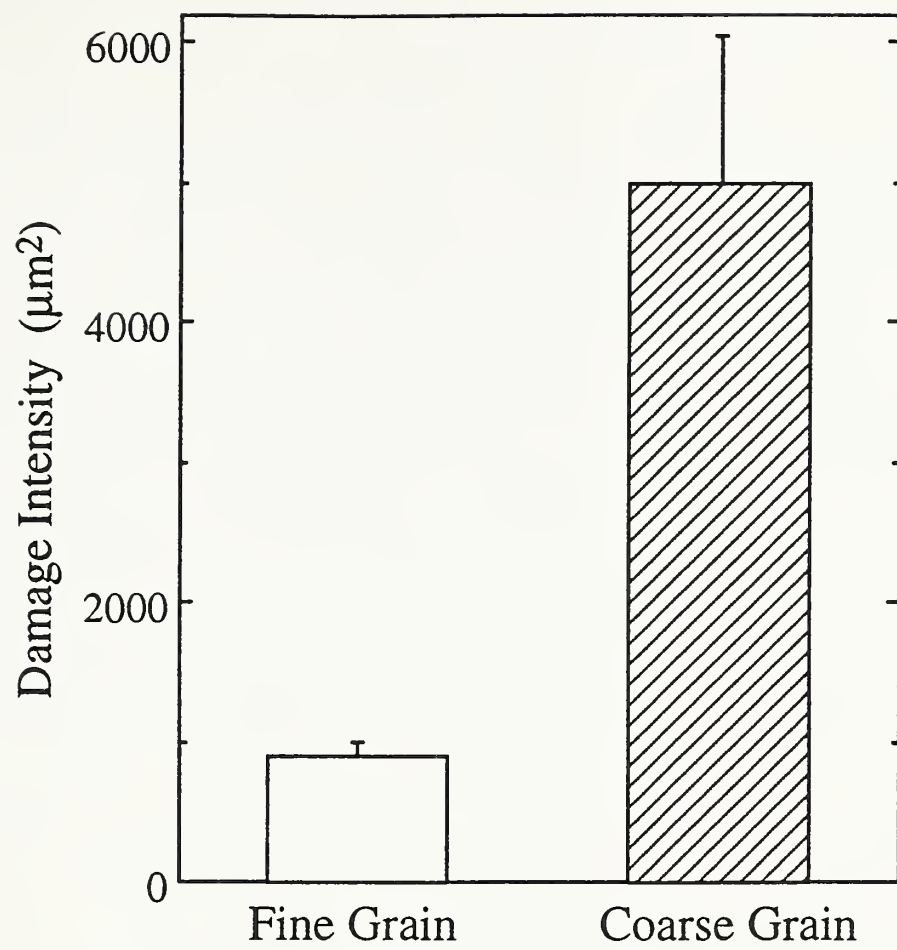


Fig. 6

